nature medicine

ARTICLES

https://doi.org/10.1038/s41591-018-0140-5

Modeling sporadic ALS in iPSC-derived motor neurons identifies a potential therapeutic agent

Koki Fujimori[1], Mitsuru Ishikawa[1], Asako Otomo[2,3,4], Naoki Atsuta[5], Ryoichi Nakamura[5], Tetsuya Akiyama[6], Shinji Hadano[2,3,7], Masashi Aoki[6], Hideyuki Saya[8], Gen Sobue[5,9] and Hideyuki Okano[1]*

Amyotrophic lateral sclerosis (ALS) is a heterogeneous motor neuron disease for which no effective treatment is available, despite decades of research into *SOD1*-mutant familial ALS (FALS). The majority of ALS patients have no familial history, making the modeling of sporadic ALS (SALS) essential to the development of ALS therapeutics. However, as mutations underlying ALS pathogenesis have not yet been identified, it remains difficult to establish useful models of SALS. Using induced pluripotent stem cell (iPSC) technology to generate stem and differentiated cells retaining the patients' full genetic information, we have established a large number of in vitro cellular models of SALS. These models showed phenotypic differences in their pattern of neuronal degeneration, types of abnormal protein aggregates, cell death mechanisms, and onset and progression of these phenotypes in vitro among cases. We therefore developed a system for case clustering capable of subdividing these heterogeneous SALS models by their in vitro characteristics. We further evaluated multiple-phenotype rescue of these subclassified SALS models using agents selected from non-*SOD1* FALS models, and identified ropinirole as a potential therapeutic candidate. Integration of the datasets acquired in this study permitted the visualization of molecular pathologies shared across a wide range of SALS models.

Amyotrophic lateral sclerosis is a neurodegenerative disorder characterized by progressive loss of upper motor neurons (UMNs) and lower motor neurons (LMNs), resulting in paralysis and death within an average of 3 to 5 years from disease onset[1]. Since the majority of ALS cases are of unknown etiology and sporadically occur in nature (90–95%), it is extremely difficult to construct disease models. Prior studies of causal genes for FALS, including superoxide dismutase 1 (*SOD1*)[2], ALS2[3], TAR DNA-binding protein of 43 kDa (*TDP-43*)[4,5], fused in sarcoma (*FUS*)[6,7], and optineurin (*OPTN*)[8], have been identified as part of several pathological cascades and phase transitions in ALS pathology[9]. While the *SOD1*^{G93A} transgenic model of ALS has provided insight into the disease mechanisms of ALS with mutations in the *SOD1* gene, the causes of motor neuron death in the most prevalent cases of SALS are still unknown. As a result of such dependence on the *SOD1* transgenic model, even after half a century of trials and testing over 150 different therapeutic agents or strategies in preclinical models of ALS, riluzole and edaravone are the only developed drugs that demonstrate slight beneficial effects in a limited population of ALS patients. Recent studies have highlighted the pathological divergence between *SOD1*-ALS and other types of ALS, including SALS[10–12], and the discrepancy between the *SOD1* mouse model and patients is one reason for the unsuccessful development of ALS therapeutics[13]. Meanwhile, the utilization of non-*SOD1* FALS models in therapeutic drug development has become a promising approach since the accumulation of abnormal protein inclusions containing specific gene products, observed in *TDP-43*- and/or *FUS*-mutated FALS, is a pathologic hallmark of SALS[14,15]. These findings indicate that there are several shared links in the pathogenesis of non-*SOD1* FALS and SALS, and compounds that suppress these common pathologic pathways may represent novel therapeutic agents for a wide range of ALS patients.

To identify the genetic factors associated with SALS, a number of genome-wide association studies using large-scale genotyping of single nucleotide polymorphisms have been conducted[16]. Unfortunately, the reported associations have not been sufficiently robust to develop disease models[17]. Additionally, in sporadic disease, the effect sizes of genetic and epigenetic factors in disease onset depend on individual cases, and there are many additional potential risk factors that have not yet been identified. Recent whole genome sequencing studies have also revealed that these sporadic cases are related to many variants, indicating cumulative genetic mutations that trigger the onset of disease[18]. Therefore, iPSC technology, which includes the complete genetic information of the donor, is a useful tool for recapitulating such heterogeneous sporadic disease pathologies in vitro[19,20]. In particular, as the majority of epigenetic modifications in donor cells are reset to the embryonic state during the reprogramming process to generate iPSCs, with the exception of epigenetic memory[21] or genetic imprinting[22], the iPSC-based cellular model demonstrates the pathologies that are primarily dependent on the genetic information for each sporadic case. Thus, to clarify the pathologies of SALS in a constantly changing epigenetic landscape, it is essential to include many cases to enable informative statistical analysis and to subdivide these cases based on their genome-derived characteristics.

[1]Department of Physiology, Keio University School of Medicine, Shinjuku-ku, Tokyo, Japan. [2]The Institute of Medical Sciences, Tokai University, Isehara, Kanagawa, Japan. [3]Department of Molecular Life Sciences, Tokai University School of Medicine, Isehara, Kanagawa, Japan. [4]Micro/Nano Technology Center, Tokai University, Hiratsuka, Kanagawa, Japan. [5]Department of Neurology, Nagoya University Graduate School of Medicine, Nagoya, Aichi, Japan. [6]Department of Neurology, Tohoku University Graduate School of Medicine, Sendai, Miyagi, Japan. [7]Research Center for Brain and Nervous Diseases, Tokai University Graduate School of Medicine, Isehara, Kanagawa, Japan. [8]Division of Gene Regulation, Institute for Advanced Medical Research, Keio University School of Medicine, Shinjuku-ku, Tokyo, Japan. [9]Research Division of Dementia and Neurodegenerative Disease, Nagoya University Graduate School of Medicine, Nagoya, Aichi, Japan. *e-mail: hidokano@a2.keio.jp

Results

Rapid and efficient motor neuron differentiation with maturation and aging. Since our previously established motor neuron differentiation protocol only produced ~10% motor neurons and required long-term culture for neural maturation and pathology reproduction[23], we first utilized culture conditions based on the direct neurosphere conversion with chemical pretreatment (CdNS)[24–26] (Supplementary Fig. 1a). After 14-day culture in modified motor neuron precursor cell (MPC) induction medium, the formed neurospheres expressed significantly up-regulated MPC markers (Supplementary Fig. 1b). Subsequently, the terminal differentiation of these neurospheres primarily resulted in motor neurons with similar expression patterns to human spinal cord samples in terms of motor-neuron- and MPC-related genes (Fig. 1a,b). In addition, due to the significant increase in motor neuron populations (Supplementary Fig. 1c), motor-neuron-specific ALS phenotypes previously reported in iPSC-derived models[23] were identified, even with a subtype-nonspecific analysis, by using this modified protocol (Supplementary Fig. 1d). Aging-related phenotypes were also accelerated using the present protocol (Supplementary Fig. 1e). Thus, we established a rapid and efficient motor neuron differentiation protocol characterized by neural maturation and aging-acceleration, hereafter referred to as CdNS-specific to motor neuron, CdNS-MN.

Identification of phase transitions in vitro for non-*SOD1* FALS pathology. Using CdNS-MN method, we generated two types of non-*SOD1* FALS models carrying *FUS* and *TDP-43* mutations. CdNS-MN was used to construct reproducible motor-neuron-enriched cultures, regardless of the iPSC line (Supplementary Fig. 1f,g). To recapitulate the in vitro transitional process of ALS pathology toward motor neuron degeneration, we evaluated time-dependent alterations of neurite outgrowth in these FALS-MNs (Fig. 1c). Whereas motor neurons from healthy donor iPSCs maintained or extended their neurites, those from *FUS*- and *TDP-43*-mutated FALS shifted to decrease their neurites at approximately 40 days in vitro (DIV) after a period of neurite outgrowth, concurrent with the formation of neurite swellings and a decrease in total neuronal cells in culture (Fig. 1d,f and Supplementary Fig. 2a–c). In addition, motor neuron ratios in culture were decreased in both *FUS*- and *TDP-43*-ALS, indicating the acceleration of motor-neuron-specific cell death with aging in vitro (Fig. 1e). Quantification of FALS neurite length alteration demonstrated the switching of neurite outgrowth toward neurite regression from DIV40 to DIV45, suggesting the phenotypic transition of in vitro FALS pathology (Fig. 1g).

To confirm the time point of the phase transition in in vitro FALS pathology, we evaluated cytotoxicity and apoptosis in iPSC-derived motor neurons by quantifying leaked lactate dehydrogenase (LDH) and immunostaining for cleaved caspase-3 (CC3). These analyses demonstrated that significant increases in both the $CC3^+$ neuron ratio and leaked LDH were observed in *TDP-43*-ALS at DIV35 and in *FUS*-ALS at DIV40 (Fig. 2a–c). Global gene expression profiling extracted 689 genes that were altered both in *FUS*- and *TDP-43*-ALS compared to those in healthy donors (Fig. 2d). Gene ontology and pathway analyses using these commonly regulated genes identified not only well-known ALS-related pathways but also unfamiliar pathways related to monoamine synthesis/degradation (Fig. 2e–g and Supplementary Table 1).

We next evaluated abnormal protein mislocalization and aggregation, focusing on gene products related to SALS pathology[14,15]. Immunostaining demonstrated an increase in the cytoplasmic mislocalization of the FUS protein in motor neurons derived from *FUS*-ALS, which was never detected in *TDP-43*-ALS (Fig. 2h,i). To characterize additional SALS-related protein aggregates, we evaluated the formation of phosphorylated TDP-43 (pTDP-43) inclusion bodies[4,5,27]. pTDP-43 aggregates in *TDP-43*-ALS motor neurons were observed in cell bodies distributed throughout the cytoplasm, which were never observed in both *FUS*-ALS and healthy donor motor neurons (Fig. 2j,k). In addition, we observed the significant increase in formed stress granules with *FUS* and *TDP-43* gene products in *FUS*- and *TDP-43*-ALS motor neurons (Fig. 2l–o). Neuronal subtype-specific analysis demonstrated that these ALS phenotypes were due to motor neurons; however, our cultures were mainly composed of motor neurons (Fig. 1a and Supplementary Figs. 1f and 3a), and these ALS phenotypes showed similar severities, detected by subtype-nonspecific pan-neuronal analysis, even without performing a motor-neuron-specific analysis (Supplementary Fig. 3b–d). Through time-course analyses of these ALS phenotypes, we found that the onset of multiple critical dysfunctions characteristic of ALS accumulated within a certain time frame in vitro (Fig. 2p and Supplementary Fig. 2d).

In vitro multi-phenotypic screening for ALS therapeutics using non-*SOD1* FALS models from iPSCs. We next performed drug screening in *FUS*- and *TDP-43*-ALS-iPSC-derived motor neurons, focusing on the transitional phase using an existing (approved) drug library comprising 1,232 drugs. Using SALS-related phenotypes observed in the non-*SOD1* FALS models as endpoints, we developed a multi-phenotypic screening system with a high-content imaging system (Fig. 3a and Supplementary Fig. 4a–c). For the primary screen, motor neurons from *FUS*-ALS iPSCs were treated with vehicle alone (0.05% (v/v) DMSO) as a control or drug dissolved in DMSO or water at a concentration of 10 μM. After 120 h, neurite lengths, the number of formed stress granules, leaked FUS aggregates, and the amount of LDH leakage were measured and evaluated as endpoints of drug efficacy (Fig. 3b,c). By comparing the common compounds selected by *FUS*-ALS models established from different iPSC clones, we identified 95 drugs that suppressed all four of the tested phenotypes of *FUS*-ALS (Fig. 3d and Supplementary Fig. 5a). For the secondary screen, motor neurons from *TDP-43*-ALS iPSCs were treated with selected 95 drugs at concentrations of 0.1, 1, or 10 μM (Fig. 3e and Supplementary Fig. 5b). By testing the same compounds selected by the FALS models, we ultimately identified nine drugs that showed positive effects on in vitro non-*SOD1* FALS phenotypes (Fig. 3f). The selected drugs were ranked by their dose-dependent effects in each phenotype expressed in motor neurons from *FUS*-ALS and *TDP-43*-ALS (Fig. 3g). Based on these data as well as the enriched gene ontology terms and pathways of the transcripts (Fig. 2e–g), detailed drug information regarding permeation through the blood-brain barrier (BBB), serious side effects, and dose-response relationships, we selected ropinirole (ROPI), which was the first or second place drug identified in both the *FUS*- and *TDP-43*-ALS models (Fig. 3g).

Ropinirole modulates decreased mitochondrial function and related pathways in non-*SOD1* FALS. ROPI is a dopamine D2 receptor (D2R) agonist used in the treatment of Parkinson's disease and restless legs syndrome[28]. Then, we first performed an evaluation of known ROPI targets using a D2R antagonist and a negative allosteric modulator (Supplementary Fig. 6a). Both the D2R antagonist and modulator only partially prevented the ROPI-mediated suppressive effect on the ALS phenotype (Supplementary Fig. 6b). In addition, the inhibitory effect of the D2R antagonist/modulator was not observed in ALS phenotypic rescue by dexpramipexole (RPPX), a structural analog of ROPI with a much lower affinity for dopamine receptors (Supplementary Fig. 6b). These results indicate that the D2R-independent mechanism is also involved in therapeutic effects of ROPI on ALS phenotypes, in addition to the D2R-mediated mechanism. Regarding its efficacy in ALS, pramipexole (PPX), another structural analog of ROPI, and RPPX, R(+) enantiomer of PPX (Supplementary Fig. 7a), have demonstrated neuroprotective effects in ALS models[29–34]. In particular, RPPX (proposed to enter mitochondria to scavenge reactive oxygen, rather than acting as a dopamine receptor agonist) has shown efficacy in

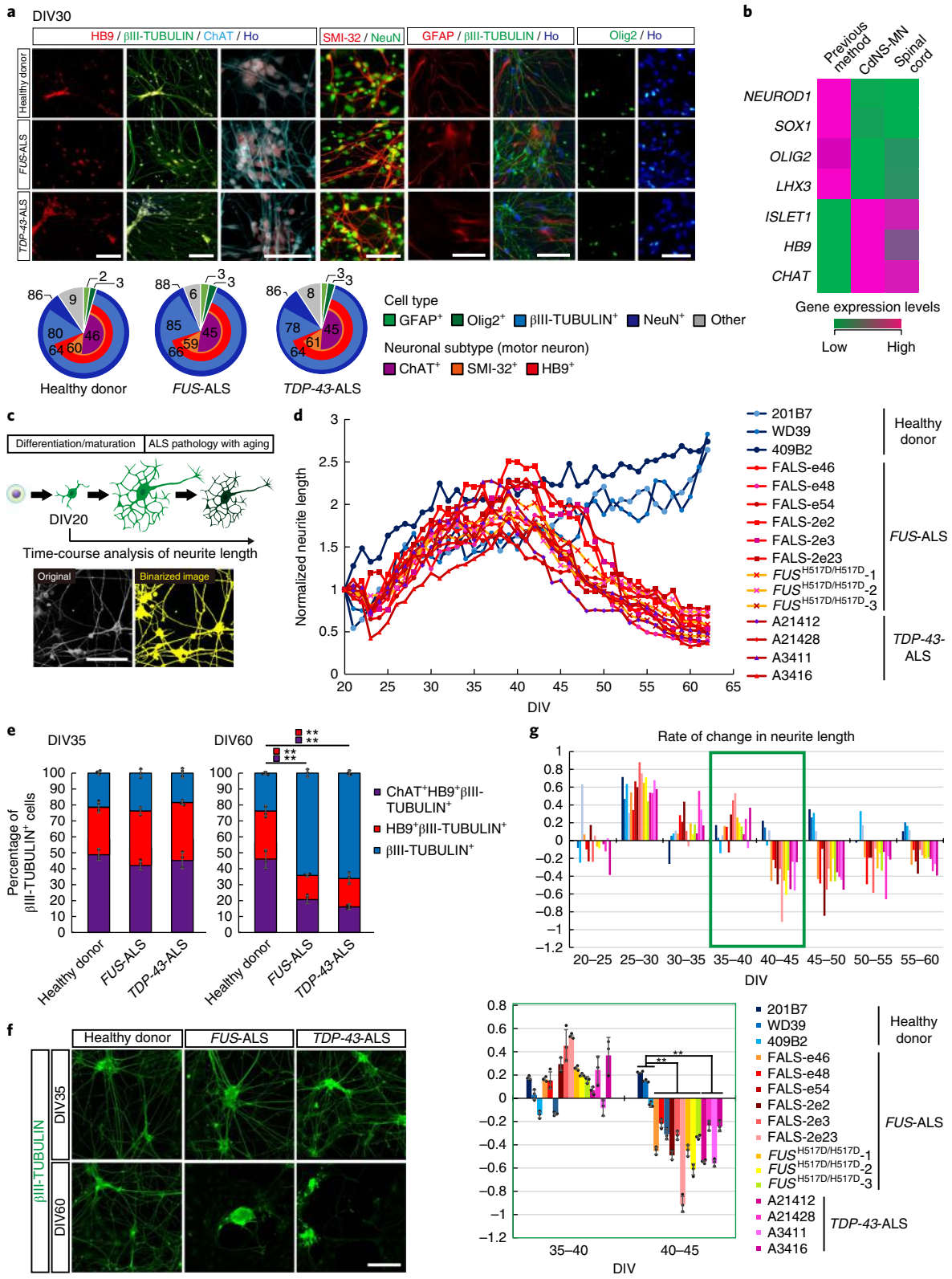

Fig. 1 | Time-course analysis of in vitro ALS pathology with aging using iPSC-derived motor neurons. a, Representative images and quantitative data of terminal differentiations using CdNS-MN. Scale bars represent 100 μm. **b**, Heatmap summary of the qPCR analysis of terminal differentiations using CdNS-MN. **c**,**d**, Neurite length analysis of motor neurons derived from healthy donor, *FUS*-ALS, and *TDP-43*-ALS iPSCs ($n = 3$ independent experiments). **e**, Quantitative analysis of the motor neuron populations in neuronal cell culture at DIV35 and DIV60 ($n = 3$ independent experiments; mean ± s.d.; $^{**}P < 0.01$; one-way ANOVA followed by Dunnett's multiple comparisons test). **f**, Representative images of neurons derived from healthy donor, *FUS*-ALS and *TDP-43*-ALS iPSCs at DIV35 and DIV60. Scale bar represents 100 μm ($n = 3$ independent experiments). **g**, Neurite length change rate every 5 days ($n = 3$ independent experiments; mean ± s.d.; $^{**}P < 0.01$; one-way ANOVA followed by Dunnett's multiple comparisons test).

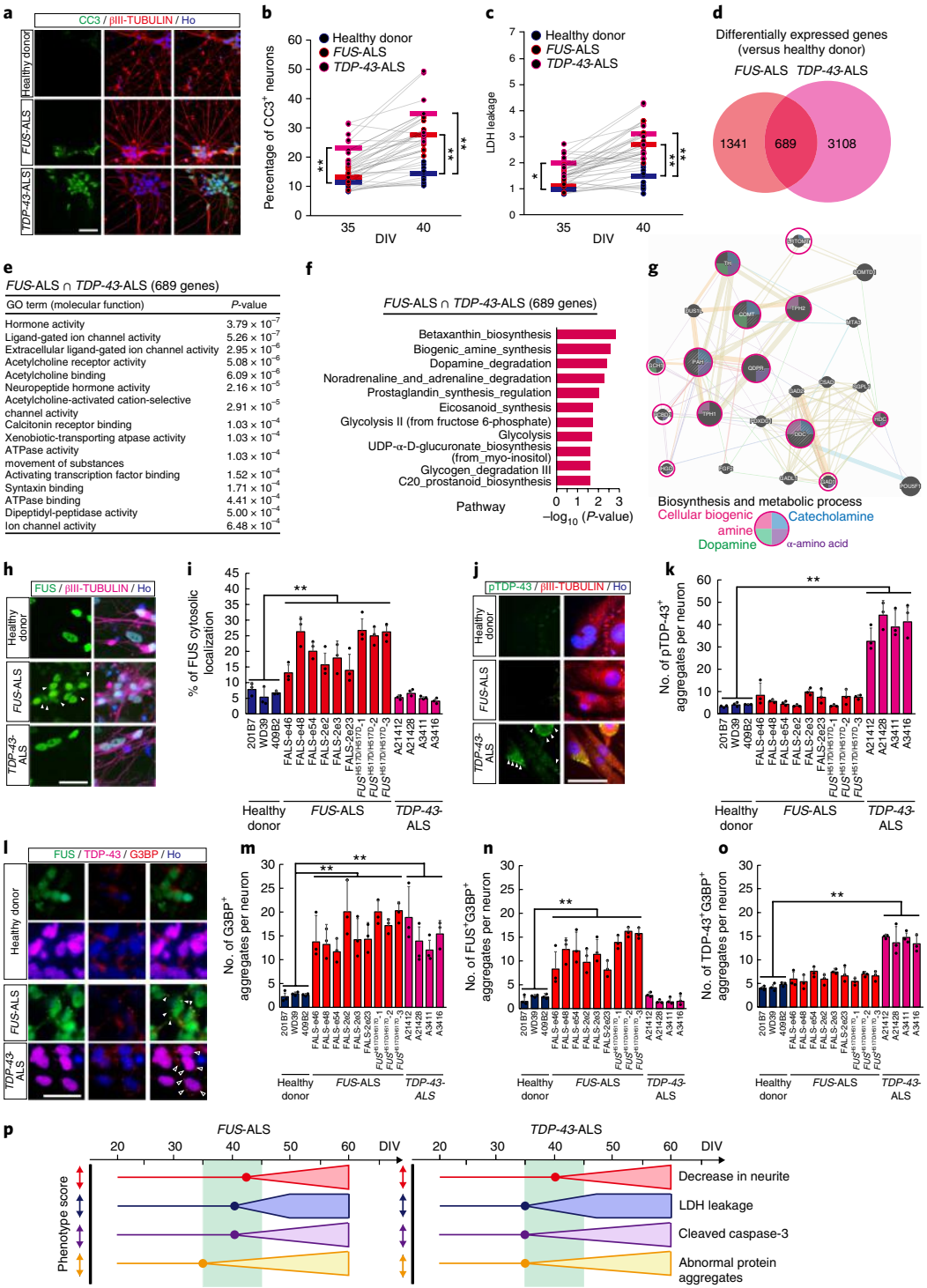

Fig. 2 | Pathological analysis of FALS models focusing on the transitional stage of in vitro pathology. a–c, Representative images and quantitative data for apoptotic and damaged neurons ($n = 3$ independent experiments; mean ± s.d.; $^{*}P < 0.05$, $^{**}P < 0.01$; one-way ANOVA followed by Dunnett's multiple comparisons test). **d**, DEGs of the transcripts of motor neurons from non-*SOD1* FALS iPSCs compared with those from healthy donor iPSCs (fold-change difference of ± 2.0; $P < 0.05$; two-tailed *t*-test). **e**, Top 15 gene ontology terms of the DEGs shown in **d** ($P < 0.05$; two-tailed Fisher's exact test). **f**, Pathway analysis of the DEGs shown in **d** ($P < 0.05$; two-tailed Fisher's exact test). **g**, Network analysis of the DEGs responsible for the top four pathways shown in **f**. **h**,**i**, FUS protein localization analysis using iPSC-derived motor neurons. Arrowheads indicate cytosolic FUS ($n = 3$ independent experiments; mean ± s.d.; $^{**}P < 0.01$; one-way ANOVA followed by Dunnett's multiple comparisons test). **j**,**k**, Representative images and quantitative data for pTDP-43 protein aggregates in iPSC-derived motor neurons ($n = 3$ independent experiments; mean ± s.d.; $^{**}P < 0.01$; one-way ANOVA followed by Dunnett's multiple comparisons test). **l–o**, Analysis of stress granule formation in iPSC-derived motor neurons. Arrowheads indicate stress granules with FUS protein, and empty arrowheads indicate stress granules with TDP-43 ($n = 3$ independent experiments; mean ± s.d.; $^{**}P < 0.01$; one-way ANOVA followed by Dunnett's multiple comparisons test). **p**, Summary of non-*SOD1* FALS phenotype transition in vitro. The alterations of each phenotype score are visualized with the data shown in Fig. 1c and Supplementary Fig. 2d. Scale bars represent 20 μm. The transcripts used from iPSC-derived motor neurons: 201B7, WD39, 409B2, and LKA10 (healthy donor); FALS-2e3 and FALS-2e23 (*FUS*-ALS); and A21412 and A21428 (*TDP-43*-ALS).

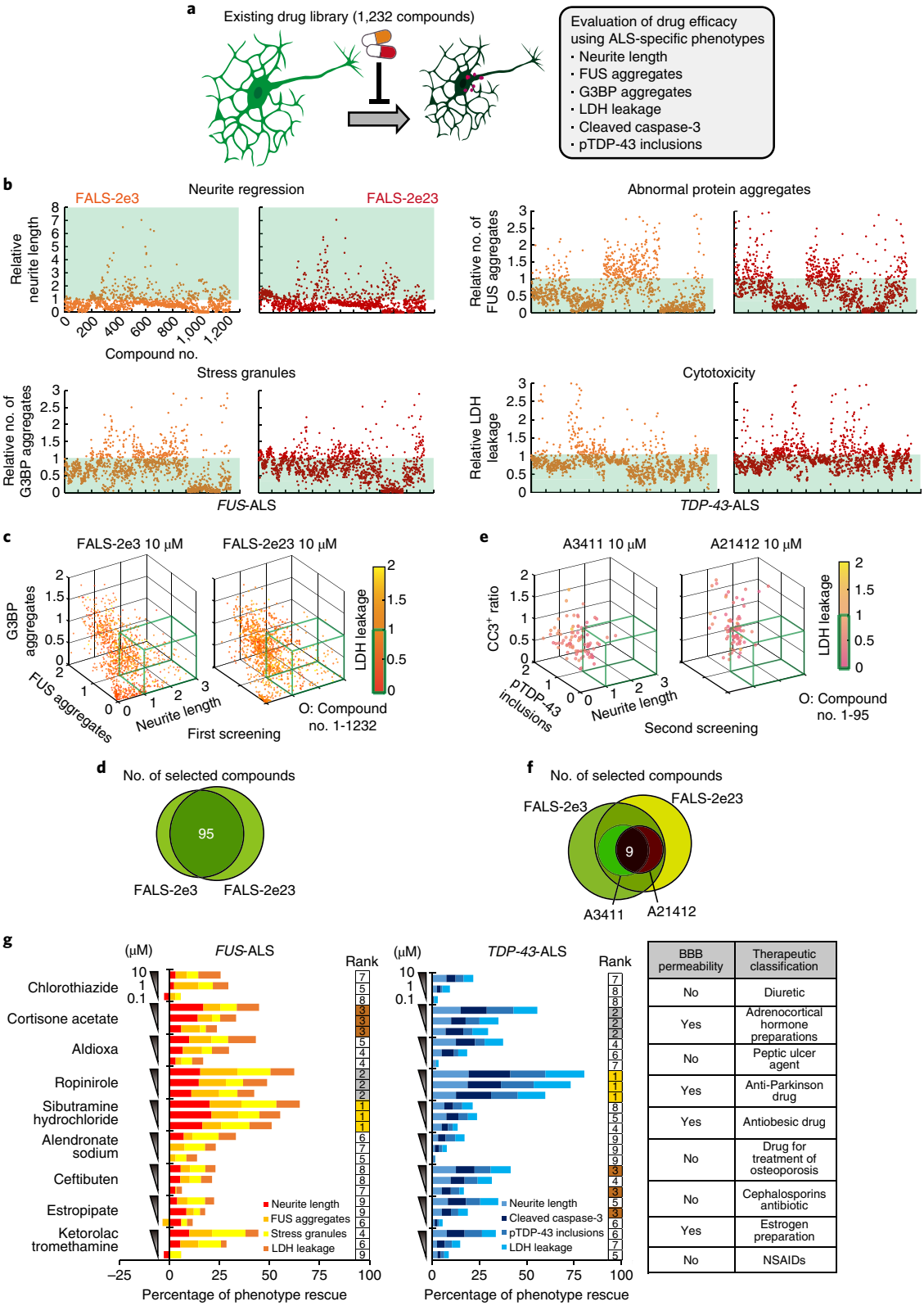

BBB permeability	Therapeutic classification
No	Diuretic
Yes	Adrenocortical hormone preparations
No	Peptic ulcer agent
Yes	Anti-Parkinson drug
Yes	Antiobesic drug
No	Drug for treatment of osteoporosis
No	Cephalosporins antibiotic
Yes	Estrogen preparation
No	NSAIDs

Fig. 3 | Multi-phenotypic screening for ALS therapeutics. a, Schematic representation of drug screening using SALS-related phenotypes of FALS carrying *FUS* and *TDP-43* mutations. **b**, Primary screening of 1,232 compounds for *FUS*-ALS-iPSC-derived motor neurons using neurite length, FUS aggregates, stress granules, and leaked LDH as endpoints. **c**, 4D-summary of primary screening in each line. Compounds showing positive effects on all of the tested endpoints are labeled in a green frame. **d**, The number of compounds selected by primary screening. **e**, Secondary screening of 95 selected compounds for motor neurons from *TDP-43*-ALS iPSCs using neurite length, pTDP-43 aggregates, CC3 ratio, and leaked LDH as endpoints. **f**, The selected compounds showing suppressive effects on in vitro pathology in FALS models carrying both *FUS* and *TDP-43* mutations. **g**, The final list of nine selected drugs and their detailed information.

preclinical studies in ALS, although it ultimately failed to show efficacy in a phase 3 clinical trial[35–38]. To validate the target of ROPI in iPSC-based ALS models, we evaluated effects of ROPI on mitochondrial activity using PPX and RPPX as controls. Pretreatment with ROPI prevented this accumulation of residual mitochondria damaged by stress (Supplementary Fig. 7b,c). In both non-SOD1 FALS models, a significant decrease in mitochondrial activity was observed before the transitional phase of in vitro pathology; ROPI treatment also suppressed this decrease (Supplementary Fig. 7d–f). In addition, the observed increase in reactive oxygen species (ROS) production in non-*SOD1* FALS-MN was prevented by ROPI treatment (Supplementary Fig. 7f). Moreover, these mitochondrial protective effects of ROPI were more potent than those of PPX and RPPX (Supplementary Fig. 7b–g). These results indicate that the additive effects of such mitochondrial protective action and the D2R-mediated action of ROPI should result in potent inhibition of ALS pathogenesis/progression in non-*SOD1*-FALS models.

In addition, ROPI treatment showed much higher improvement in in vitro disease conditions compared to existing ALS therapeutic agents and previously tested agents for ALS clinical trials (Supplementary Fig. 6c). However, ROPI did not show any suppressive effects on the phenotypes in *SOD1*-mutant iPSC-derived motor neurons, except for mitochondrial dysfunction (Supplementary Fig. 8a–i and Supplementary Table 2). Network analysis of the transcripts demonstrated that several factors and pathways, including mitochondrial electron transport system, were affected by ROPI (Supplementary Fig. 9d,e). Additionally, in *SOD1*-ALS, the genes and pathways affected by ROPI treatment were significantly different from those of non-*SOD1* FALS although the monoamine-related pathways were commonly altered in FALS regardless of *SOD1* mutation (Supplementary Fig. 9b–e). These results indicate that ROPI certainly has a potent mitochondrial protective effect and mitochondrial dysfunction associates with the complex FALS pathological processes, however, the subsequent motor neuron atrophy might be caused by the different paths between *SOD1*-ALS and non-*SOD1* ALS.

iPSC-based multi-patient SALS models and their phenotypic clustering recapitulate clinical features. To resolve the problem of heterogeneity in SALS cases and evaluate the efficacy of the selected drug in a wide range of ALS cases, we established multi-patient iPSC models in bulk from lymphoblastoid B cell lines (LCLs) of 32 SALS patients[39–41]. To evaluate the usefulness of our bulk culture system, we compared two culture systems with or without colony picking using iPSCs from 10 SALS patients; no significant differences were demonstrated between the two culture systems (Supplementary Fig. 10a–e). All 32 bulk-established SALS-iPSCs expressed pluripotent markers, differentiated into all three germ layer cells via embryoid bodies, and induced differentiation toward motor neurons without bias using CdNS-MN (Supplementary Fig. 10f–l). In sporadic diseases, the effect sizes of genetic and epigenetic factors in disease onset depend on individual cases; therefore, it is necessary to classify heterogeneous SALS to understand their pathologies (Fig. 4a). When we first performed a time-course analysis of neurite outgrowth and the LDH assay because markers indicated the cells were approaching cell death, the behavior of each SALS case was vastly different, although a high correlation was observed between the two assays for each case (Fig. 4b,c). The majority of in vitro cases expressing phenotypes with shorter culture periods were LMN-onset SALS patients (Fig. 4d,e). Although there was no correlation between the culture period of these cell death-related phenotype expression in vitro and clinical ALS onset age (Fig. 4e), in vitro case clustering based on such phenotypes (Supplementary Fig. 11) indicated the correspondence between disease progression in vitro and clinical SALS classification with amyotrophic lateral sclerosis functional rating scale (ALSFRS-R)[41]; the majority of the clinically "Moderate" type of SALS patients was classified into the moderate progression cluster of in vitro pathology (Cluster-4) in their iPSC-based models (Fig. 4f,g). This SALS case classification with our in vitro disease progression also showed correspondence with the clinical time period until the initiation of mechanical ventilation after ALS onset; these clinical periods were significantly longer in the SALS patients classified within in vitro Cluster-4 than those in the patients within the other three clusters (Fig. 4h). This case-specific clinical period was also correlated with our in vitro survival/ALS progression period with the alteration in neurite length (Supplementary Fig. 12a–c). These data strongly suggest a certain association between pathological progress in clinical and iPSC-based models, even in sporadic diseases. Furthermore, quantitative analysis of abnormal protein aggregation characterized by *FUS*-ALS and *TDP-43*-ALS clarified that SALS also expressed these phenotypes, although the extent of these phenotypes significantly varied depending on the individual sporadic case, and the majority of these phenotypes were accompanied by cytosolic aggregation of the TDP-43 protein (Fig. 4i,j and Supplementary Fig. 11). In contrast, *SOD1* pathologies were rarely observed in SALS models (Fig. 4i,j). These non-*SOD1* ALS phenotypes were similarly confirmed in pathological models established from colony-picked SALS-iPSCs, strongly indicating that the ALS phenotypes detected in the SALS models were due to genetic information (Supplementary Fig. 13a–d). Motor neuron specificity was also observed for these SALS phenotypes; however, because of the use of motor-neuron-enriched cultures (Supplementary Fig. 10l), as in FALS, the severities detected by subtype-nonspecific analysis were comparable to those determined by a motor-neuron-specific analysis (Supplementary Fig. 13e–g). Based on the in vitro progression of ALS pathology and abnormal protein aggregation characterized by specific genetic mutations in FALS, we ultimately visualized the significant differences in each SALS case via three-dimensional case distributions of in vitro SALS models (Fig. 4k and Supplementary Fig. 11).

Drug-based in vitro subdivision of SALS cases and identification of a therapeutic agent effective in both FALS and SALS models. For the efficacy evaluation of ROPI, we selected 24 SALS models with our in vitro case clustering (22 SALS models; in vitro disease progression cluster-1, -2, and -3: two SALS models; in vitro disease progression cluster-4, with higher FUS- and/or TDP-43-ALS phenotype score than the average) (Figs. 4f–k and 5a). Apoptosis induction were enhanced in 22 cases of the selected ones at the transitional phase of in vitro pathology specific to each patient (Fig. 5a–c). ROPI treatment of these 22 SALS cases significantly suppressed apoptosis induction in 16 cases (Fig. 5b,c). ROPI also suppressed the ROS increase in these 16 cases, irrespective of its improvement effect in all 22 SALS models of mitochondrial dysfunction (Supplementary Fig. 14a–d). In addition to apoptosis and ROS, ROPI suppressed neuronal atrophy, abnormal protein aggregation, and cytotoxicity in most of the SALS models (Fig. 5d). Of the nine compounds selected by non-*SOD1* FALS screening, ROPI was effective in the highest number of SALS cases compared to the other eight compounds (Fig. 5e). Furthermore, when SALS cases were analyzed by FALS-based subdivision, the majority of the ROPI-responder SALS cases clearly expressed *FUS*- and/or *TDP-43* phenotypes in vitro (Fig. 5f).

Based on the data obtained from our drug efficacy evaluation, which was consistent with the results of three-dimensional case clustering in vitro (Fig. 6a), characteristic phenotype data related to FALS-responsible genes (Fig. 5f), disease progression in vitro, and clinical information, four representative SALS cases were selected (SALS-12, SALS-14, SALS-17, and SALS-30) (Fig. 6b and Supplementary Table 3). Comparative analysis using the transcripts of these models demonstrated that SALS-12, which did not show ROPI reactivity, exhibited a gene expression pattern similar to that of *SOD1*-ALS models compared with other SALS cases (Fig. 6c). Pathway analysis of the differentiated expression genes (DEGs)

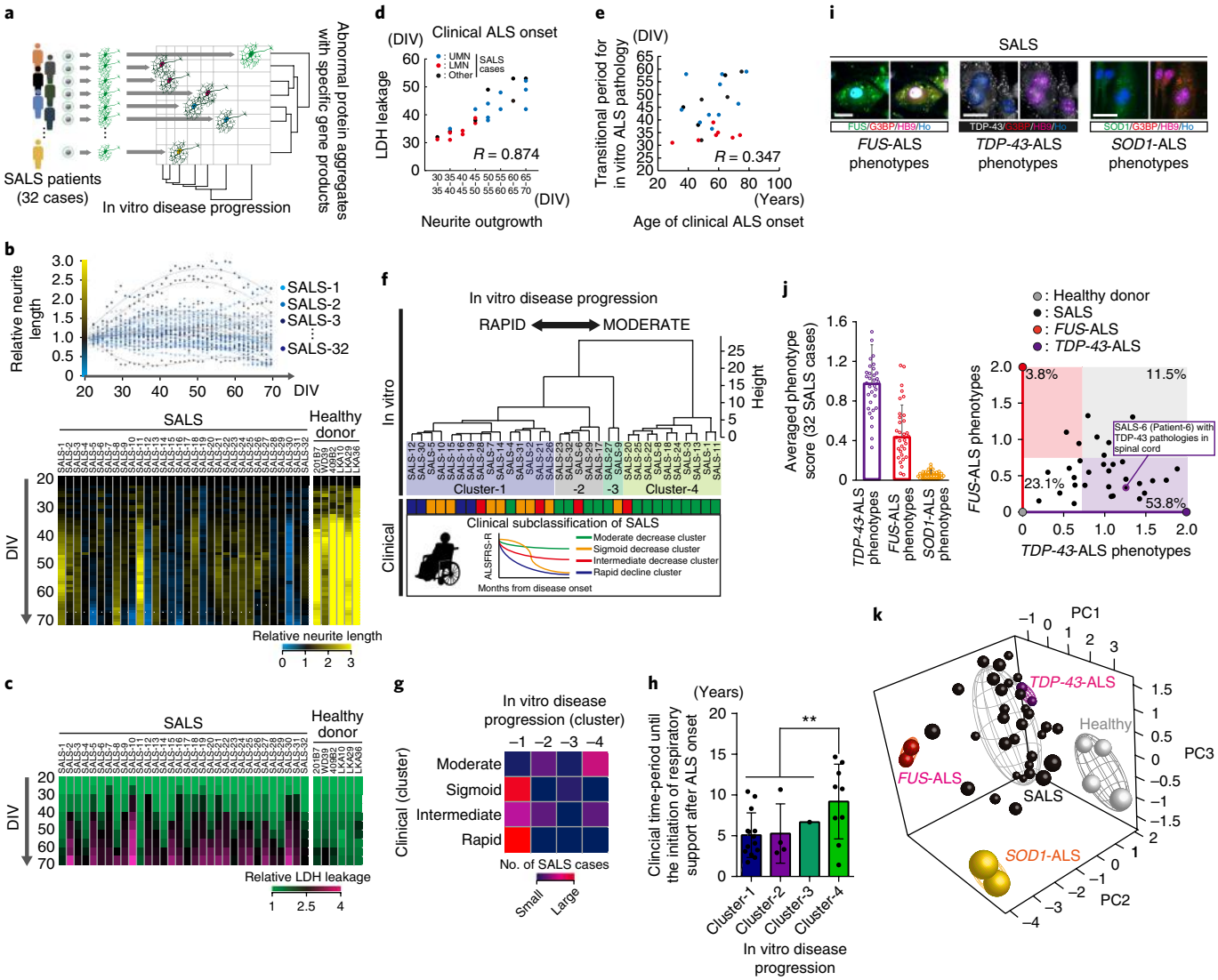

Fig. 4 | Pathological analysis and phenotype-based clustering of multiple SALS models. a, Schematic representation of phenotype-based case clustering ($n=3$ independent experiments). **b**, Neurite length analysis of motor neurons derived from 32 SALS-iPSCs. **c**, Analysis of cell damage using motor neurons derived from 32 SALS-iPSCs ($n=3$ independent experiments). **d**, Pearson's correlation analysis of in vitro phenotype onset between neurite outgrowth and LDH leakage using 32 SALS models. **e**, Pearson's correlation analysis of in vitro phenotype onset and clinical ALS onset in 32 SALS patients. SALS patients were classified clinically by UMN onset, LMN onset, or other. **f**, Hierarchical clustering of in vitro phenotype progression of motor neurons derived from 32 SALS-iPSCs using the datasets shown in **b** and **c**. The clustering shows a high correlation with clinical SALS case classification based on ALSFRS-R clinical variation mode. **g**, Heatmap summary of the corresponding relationship between the in vitro disease progression cluster and the clinical subclassification of SALS patients. **h**, Clinical time period until the initiation of respiratory support after ALS onset of SALS patients in each in vitro disease progression cluster, including the data of deceased SALS patients and living SALS patients more than 5 years after onset without respiratory support ($n=14$ (Cluster-1); $n=4$ (Cluster-2); $n=1$ (Cluster-3); $n=9$ (Cluster-4); mean ± s.d.; $^{**}P<0.01$; two-tailed t-test). **i**, Representative images of abnormal protein aggregates and cytosolic mislocalization in neurons derived from SALS-iPSCs. **j**, Multi-phenotypic clustering of 32 SALS models characterized by phenotypes of *FUS*-ALS, *TDP-43*-ALS, and *SOD1*-ALS ($n=3$ independent experiments; mean ± s.d.: the thresholds of each phenotype score are set at 0.75). **k**, PCA-based subclassification of in vitro SALS cases using their phenotype progression and characterized phenotypes ($n=3$ independent experiments). See Methods for details.

extracted by comparing each SALS model and healthy donors clarified that inflammation-related pathways and dopamine-related pathways, whose changes were observed in FALS models (Fig. 2e–g and Supplementary Fig. 9a–c), would also affect SALS pathologies (Fig. 6d). As a result of extracting the pathways by classifying SALS cases with ROPI reactivity, fatty acids and their related behaviors were extracted (Fig. 6e). Similarly, the transcriptome analysis of SALS and FALS models following ROPI treatment revealed that many pathways extracted from commonly altered gene sets involve dopamine (Fig. 6f and Supplementary Fig. 15a,b). These results support our finding that the neuroprotective effects of ROPI against non-*SOD1*-FALS pathologies were partially due to the action mediated by the dopamine receptor (Supplementary Fig. 6a,b) and suggest that the D2R-mediated action of this drug affects the pathology of SALS cases with ROPI reactivity. More detailed analysis of the gene sets that were specifically altered in ROPI-responder SALS models identified an increase in eicosanoid biosynthesis and a decrease in the statin pathway, which regulates the biosynthesis of mevalonate and, subsequently, cholesterol, with ROPI treatment (Fig. 6f). Given the significant increase in ROS in ROPI-responder

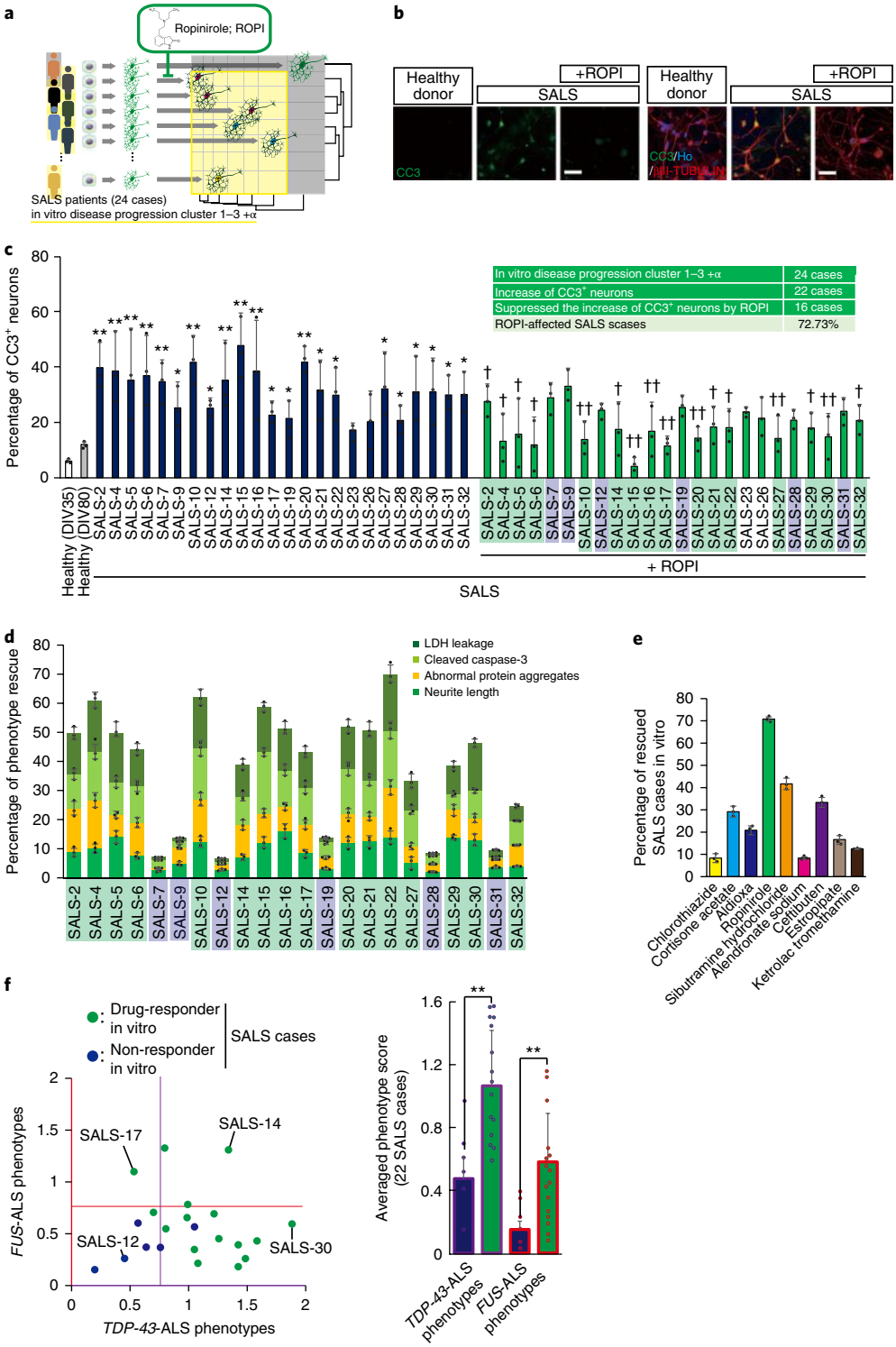

Fig. 5 | Evaluation of drug efficacy using multiple SALS models. a, Schematic representation of the evaluation of ROPI efficacy for 24 SALS models mainly included in in vitro disease progression cluster-1, -2, and -3. **b**,**c**, Representative images and quantitative data for apoptotic neurons from 24 SALS models. ROPI significantly prevented the induction of apoptosis in 16 SALS cases among 22 cases observed to demonstrate an increase in apoptosis ($n=3$ independent experiments; mean ± s.d.; $^{*}P<0.05$, $^{**}P<0.01$ when comparing healthy donor and SALS; one-way ANOVA followed by Dunnett's multiple comparisons test, $\dagger P<0.05$. $\dagger\dagger P<0.01$ when comparing untreated SALS and ROPI-treated SALS; two-tailed *t*-test). Scale bar represents 20 μm. **d**, Evaluation of ROPI efficacy in 22 SALS models with multiple ALS-related phenotypes ($n=3$ independent experiments; mean ± s.d.). **e**, Efficacy evaluation of the screened nine drug candidates for ALS therapeutics using 22 SALS models. Four ALS phenotypes were used as endpoints: neurite regression, apoptosis, abnormal protein aggregates, and cytotoxicity. To adjust the maximum value of phenotype rescue to 100% when accumulating four endpoints, the upper limit of phenotype rescue for each item was compressed to 25%. Rescued in vitro cases with phenotype rescue scores > 25% ($n=3$ independent experiments; mean ± s.d.). **f**, In vitro characterization of ROPI-responsive SALS cases based on FALS phenotypic clustering ($n=3$ independent experiments; mean ± s.d.; $^{**}P<0.01$; two-tailed *t*-test).

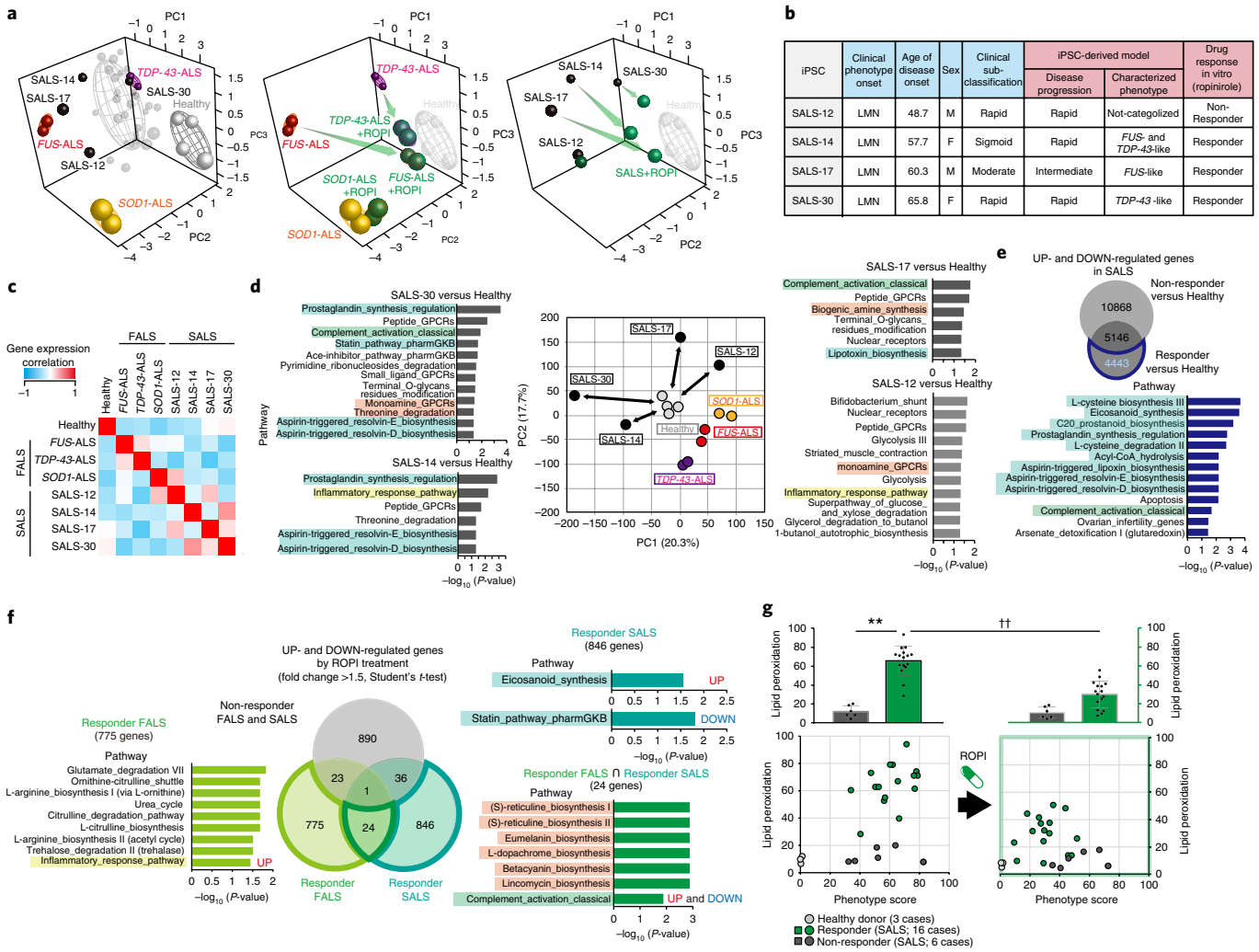

Fig. 6 | Transcriptional characterization of SALS models and identification of ROPI target pathways using in vitro multi-phenotypic case classification. **a**, Drug efficacy evaluation for three-dimensional subclassified SALS and FALS models based on their in vitro phenotypes ($n = 3$ independent experiments). **b**, Details of selected four SALS models with characterized in vitro phenotypes and drug responsiveness. **c**, Pearson's correlation analysis of the transcripts of iPSC-derived motor neurons derived from healthy donors, FALS patients, and SALS patients. **d**, PCA of the transcripts and enriched pathways of DEGs in each SALS model compared with that in healthy donors (a fold-change difference of ±2.0; two-tailed *t*-test). **e**, Summary of the enriched pathways of DEGs among SALS models shown in **d** focusing on drug responsiveness ($P < 0.05$; two-tailed Fisher's exact test). **f**, Venn diagram and enriched pathways of DEGs following ROPI treatment, focusing on drug responsiveness and ALS-related genetic background (a fold-change difference of ±1.5; two-tailed *t*-test). **g**, In vitro lipid peroxidation analysis and drug efficacy evaluation of ROPI in 22 SALS models with ALS-related phenotypes. Lipid peroxidation represents the relative value of the MDA concentration with the healthy donor group as a reference value. Phenotype score is composed of quantified ALS-related phenotypes detected in 22 SALS models, specifically LDH leakage, $CC3^+$ ratio increase, abnormal protein aggregates, and neurite decrease, and represents an integrated value ($n = 3$ independent experiments; mean ± s.d.; $^{**}P < 0.01$ when comparing non-responder and responder; $^{††}P < 0.01$ when comparing untreated responder and ROPI-treated responder; one-way ANOVA followed by Tukey's multiple comparisons test). The transcripts of iPSC-derived motor neurons used: 201B7, WD39, 409B2, and LKA10 (healthy donor); FALS-2e3 and FALS-2e23 (*FUS*-ALS); A21412 and A21428 (*TDP-43*-ALS); 1-SOD1-4 and 2-SOD1-4 (*SOD1*-ALS); SALS-12, SALS-14, SALS-17, and SALS-30 (SALS); ROPI-treated cells.

SALS compared with that in non-responder SALS (Supplementary Fig. 14d) as well as the gene- and case-dependent divergence in ROPI responsiveness to in vitro ALS phenotypes (Fig. 6f and Supplementary Figs. 7a–g, 8d–i, and 13a,13c) and the networks of DEGs identified in SALS with drug responsiveness (Supplementary Fig. 16a,b), the present study also focused on fatty acid-related pathways, particularly lipid peroxidation, which is modulated by mevalonate pathway[42]. Additionally, the effects of lipid peroxidation on aging and the pathogenic/progressive processes of neurodegenerative diseases, including ALS, have been actively studied[43,44]. Then, we quantified the end products of lipid peroxidation, and detected a significant increase in malondialdehydes (MDAs) in 22 SALS models with definite ALS pathology (Fig. 6g). In addition, the enhancement of lipid peroxidation was suppressed by ROPI treatment, specifically in the responder group (Fig. 6g). These results strongly indicate that the fatty acid-related oxidation process is involved in ALS onset and progression, especially for SALS, and by modulating relevant pathways, except for dopamine-related pathways, ROPI exerted therapeutic effects on a wide range of ALS models, regardless of their genetic background.

Discussion

In the present study, we established SALS models of multiple patients using iPSC technology and recapitulated the patients'

genetic and clinical heterogeneity in vitro. Although phenotypic differences were partly suggested in previous iPSC-based studies for a small number of SALS cases, iPSC models have never been used to address the heterogeneity among SALS cases, and their usefulness as disease models has not been fully verified[45–47]. Using multiple-patient SALS models, this study demonstrates two advantages in understanding ALS pathologies and developing therapeutic drugs. First, genetically and clinically heterogeneous SALS patients were subdivided according to their in vitro characteristics by iPSC modeling. Since these subclassifications were correlated with both clinical disease progression and features of their clinical characteristics, we clearly demonstrated that iPSC technology enabled the generation of elaborate disease models that accurately reflect the clinical features of genetic conditions, even sporadic diseases. These findings also suggest the applicability of our case cluster model to predict clinical ALS progress, and therefore the expected usability is high. Second, drug candidates effective for both FALS and SALS were identified by our multi-phenotypic analysis/screening system. In ALS, whose detailed pathological processes are still unknown, despite the identification of several representative phenotypes[48], the present model is an effective approach for the development of ALS therapeutics to comprehensively reproduce ALS phenotypes and screen compounds that show efficacy in all disease phenotypes. Here, the ALS drug candidate ROPI identified by our multi-phenotypic assay system showed protective effects not only in *FUS*- and *TDP-43*-mutated FALS models but also in the majority of SALS models. Therefore, these results highlight the potential utility of ROPI as an ALS therapeutic targeting a wide range of clinical cases.

However, in *SOD1*-mutant ALS models, which suggest substantial differences in SALS pathologies[49], ROPI did not suppress the detected phenotypes (Supplementary Fig. 8d,f–h). Based on these variations in ROPI reactivity caused by the genetic backgrounds of ALS patients, we clarified the differences in molecular behaviors involved in ALS pathology. In particular, in both familial and non-*SOD1* sporadic ALS groups showing significant ROPI reactivity, several dopamine-related pathways were commonly regulated by ROPI treatment. A previous IPT single photon emission computed tomography (SPECT)-based dopamine transporter imaging study showed that nigrostriatal dopaminergic neurons were subclinically affected in a subset of patients with SALS[50]. In recent studies, dopamine itself has been reported to regulate the function of spinal motor neurons[51,52] and promote their adult regeneration[53]. These reports strongly support our findings using motor-neuron-enriched culture without dopaminergic neurons (Supplementary Fig. 1g), and the abnormalities of dopamine-mediated effects on motor neurons might affect the promotion of ALS pathology in motor neurons. Furthermore, we demonstrated that ROPI exerts stronger neuroprotective effects than RPPX, and a portion of this effect of ROPI is mediated by dopamine receptors (Supplementary Fig. 6a,b). These results are consistent with the fact that RPPX, which presents much lower affinity for dopaminergic receptors, shows no significant therapeutic effects on clinical ALS patients[38], whereas we strongly expect ROPI to show clinical usefulness. The fatty acid-related pathways specifically altered in the SALS group with ROPI reactivity have also been implicated in ALS pathologies, and increased lipid peroxidation has been confirmed in sera of SALS patients[42,54]. Additionally, Chen and colleagues demonstrated that lipid peroxidation and mitochondrial dysfunction were involved in motor neuron ferroptosis both in vivo and in vitro, and ablation of the ferroptosis inhibitor glutathione peroxidase 4 in neurons caused rapid motor neuron degeneration and paralysis[55]. Since an increase in CC3-positive motor neurons was also observed in our 22 SALS models, the mechanism leading to motor neuron degeneration appears to be complex. However, as shown in Fig. 6g, it is clear that lipid peroxidation and subsequent ferroptosis play an important role in motor neuron degeneration in the majority of SALS models.

Here, we generated motor neurons from ALS patient-derived iPSCs. However, in ALS pathogenesis, non-cell autonomous mechanisms have been well characterized[48]. By focusing on motor-neuron-enriched cultures in the present study, our pathological analysis and screening method guaranteed robustness and scalability, but the contributions of other cell types were not considered. Establishment of a multi-cellular model more closely mimicking the spinal cord would be another effective approach to understand the non-cell autonomous pathologies of heterogeneous ALS patients.

These results support the sufficient utility of SALS models for elucidating the pathological characteristics of specific cases and identifying novel candidate drugs. In addition, our iPSC-based analysis/clustering/screening system is applicable not only to SALS but also to other sporadic neurodegenerative diseases, such as Parkinson's disease and Alzheimer's disease. Thus, the present study provides a novel paradigm of sporadic neurologic disease modeling and contributes new insights to SALS pathology and therapeutic agent development.

Methods

Methods, including statements of data availability and any associated accession codes and references, are available at https://doi.org/10.1038/s41591-018-0140-5.

Received: 28 November 2017; Accepted: 11 July 2018;
Published online: 20 August 2018

References

1. Zinman, L. & Cudkowicz, M. Emerging targets and treatments in amyotrophic lateral sclerosis. *Lancet Neurol.* **10**, 481–490 (2011).
2. Rosen, D. R. et al. Mutations in Cu/Zn superoxide dismutase gene are associated with familial amyotrophic lateral sclerosis. *Nature* **362**, 59–62 (1993).
3. Hadano, S. et al. A gene encoding a putative GTPase regulator is mutated in familial amyotrophic lateral sclerosis 2. *Nat. Genet.* **29**, 166–173 (2001).
4. Arai, T. et al. TDP-43 is a component of ubiquitin-positive tau-negative inclusions in frontotemporal lobar degeneration and amyotrophic lateral sclerosis. *Biochem. Biophys. Res. Commun.* **351**, 602–611 (2006).
5. Neumann, M. et al. Ubiquitinated TDP-43 in frontotemporal lobar degeneration and amyotrophic lateral sclerosis. *Science* **314**, 130–133 (2006).
6. Kwiatkowski, T. J.Jr et al. Mutations in the FUS/TLS gene on chromosome 16 cause familial amyotrophic lateral sclerosis. *Science* **323**, 1205–1208 (2009).
7. Vance, C. et al. Mutations in FUS, an RNA processing protein, cause familial amyotrophic lateral sclerosis type 6. *Science* **323**, 1208–1211 (2009).
8. Maruyama, H. et al. Mutations of optineurin in amyotrophic lateral sclerosis. *Nature* **465**, 223–226 (2010).
9. Da Cruz, S. & Cleveland, D. W. Understanding the role of TDP-43 and FUS/TLS in ALS and beyond. *Curr. Opin. Neurobiol.* **21**, 904–919 (2011).
10. Liu, H. N. et al. Lack of evidence of monomer/misfolded superoxide dismutase-1 in sporadic amyotrophic lateral sclerosis. *Ann. Neurol.* **66**, 75–80 (2009).
11. Kabashi, E. et al. FUS and TARDBP but not SOD1 interact in genetic models of amyotrophic lateral sclerosis. *PLoS Genet.* **7**, e1002214 (2011).
12. Da Cruz, S. et al. Misfolded SOD1 is not a primary component of sporadic ALS. *Acta Neuropathol.* **134**, 97–111 (2017).
13. Philips, T. & Rothstein, J. D. Rodent models of amyotrophic lateral sclerosis. *Curr. Protoc. Pharmacol.* **69**, 5.67.61–21 (2015).
14. Mizusawa, H. et al. Focal accumulation of phosphorylated neurofilaments within anterior horn cell in familial amyotrophic lateral sclerosis. *Acta Neuropathol.* **79**, 37–43 (1989).
15. Okamoto, K., Hirai, S., Ishiguro, K., Kawarabayashi, T. & Takatama, M. Light and electron microscopic and immunohistochemical observations of the Onuf's nucleus of amyotrophic lateral sclerosis. *Acta Neuropathol.* **81**, 610–614 (1991).
16. Renton, A. E., Chio, A. & Traynor, B. J. State of play in amyotrophic lateral sclerosis genetics. *Nat. Neurosci.* **17**, 17–23 (2014).
17. Iida, A. et al. Replication analysis of SNPs on 9p21.2 and 19p13.3 with amyotrophic lateral sclerosis in East Asians. *Neurobiol. Aging* **32**, 757.e713–754 (2011).
18. Manolio, T. A. et al. Finding the missing heritability of complex diseases. *Nature* **461**, 747–753 (2009).
19. Mattis, V. B. & Svendsen, C. N. Induced pluripotent stem cells: a new revolution for clinical neurology?. *Lancet Neurol.* **10**, 383–394 (2011).
20. Okano, H. & Yamanaka, S. iPS cell technologies: significance and applications to CNS regeneration and disease. *Mol. Brain* **7**, 22 (2014).

21. Kim, K. et al. Epigenetic memory in induced pluripotent stem cells. *Nature* **467**, 285–290 (2010).
22. Okuno, H. et al. Changeability of the fully methylated status of the 15q11.2 region in induced pluripotent stem cells derived from a patient with Prader–Willi syndrome. *Congenit. Anom. (Kyoto)* **57**, 96–103 (2017).
23. Ichiyanagi, N. et al. Establishment of in vitro FUS-associated familial amyotrophic lateral sclerosis model using human induced pluripotent stem cells. *Stem Cell Reports* **6**, 496–510 (2016).
24. Fujimori, K. et al. Escape from pluripotency via inhibition of TGF-β/BMP and activation of wnt signaling accelerates differentiation and aging in hPSC progeny cells. *Stem Cell Reports* **9**, 1675–1691 (2017).
25. Fujimori, K. et al. Modeling neurological diseases with induced pluripotent cells reprogrammed from immortalized lymphoblastoid cell lines. *Mol. Brain* **9**, 88 (2016).
26. Matsumoto, T. et al. Functional neurons generated from T cell-derived induced pluripotent stem cells for neurological disease modeling. *Stem Cell Reports* **6**, 422–435 (2016).
27. Guo, W. et al. An ALS-associated mutation affecting TDP-43 enhances protein aggregation, fibril formation and neurotoxicity. *Nat. Struct. Mol. Biol.* **18**, 822–830 (2011).
28. Kuzel, M. D. Ropinirole: a dopamine agonist for the treatment of Parkinson's disease. *Am. J. Health Syst. Pharm.* **56**, 217–224 (1999).
29. Abramova, N. A., Cassarino, D. S., Khan, S. M., Painter, T. W. & Bennett, J. PJr.. Inhibition by R(+) or S(−) pramipexole of caspase activation and cell death induced by methylpyridinium ion or beta amyloid peptide in SH-SY5Y neuroblastoma. *J. Neurosci. Res.* **67**, 494–500 (2002).
30. Danzeisen, R. et al. Targeted antioxidative and neuroprotective properties of the dopamine agonist pramipexole and its nondopaminergic enantiomer SND919CL2x [(+)2-amino-4,5,6,7-tetrahydro-6-Lpropylamino-benzathiazole dihydrochloride]. *J. Pharmacol. Exp. Ther.* **316**, 189–199 (2006).
31. Ferrari-Toninelli, G., Maccarinelli, G., Uberti, D., Buerger, E. & Memo, M. Mitochondria-targeted antioxidant effects of S(−) and R(+) pramipexole. *BMC Pharmacol.* **10**, 2 (2010).
32. Gu, M. et al. Pramipexole protects against apoptotic cell death by non-dopaminergic mechanisms. *J. Neurochem.* **91**, 1075–1081 (2004).
33. Sethy, V. H., Wu, H., Oostveen, J. A. & Hall, E. D. Neuroprotective effects of the dopamine agonists pramipexole and bromocriptine in 3-acetylpyridine-treated rats. *Brain Res.* **754**, 181–186 (1997).
34. Cassarino, D. S., Fall, C. P., Smith, T. S. & Bennett, J. P.Jr.. Pramipexole reduces reactive oxygen species production in vivo and in vitro and inhibits the mitochondrial permeability transition produced by the parkinsonian neurotoxin methylpyridinium ion. *J. Neurochem.* **71**, 295–301 (1998).
35. Wang, H. et al. R+pramipexole as a mitochondrially focused neuroprotectant: initial early phase studies in ALS. *Amyotroph. Lateral Scler.* **9**, 50–58 (2008).
36. Cheah, B. C. & Kiernan, M. C. Dexpramipexole, the R(+) enantiomer of pramipexole, for the potential treatment of amyotrophic lateral sclerosis. *IDrugs* **13**, 911–920 (2010).
37. Corcia, P. & Gordon, P. H. Amyotrophic lateral sclerosis and the clinical potential of dexpramipexole. *Ther. Clin. Risk Manag.* **8**, 359–366 (2012).
38. Cudkowicz, M. E. et al. Dexpramipexole versus placebo for patients with amyotrophic lateral sclerosis (EMPOWER): a randomised, double-blind, phase 3 trial. *Lancet Neurol.* **12**, 1059–1067 (2013).
39. Iida, A. et al. A functional variant in ZNF512B is associated with susceptibility to amyotrophic lateral sclerosis in Japanese. *Hum. Mol. Genet.* **20**, 3684–3692 (2011).
40. Nakamura, R. et al. Neck weakness is a potent prognostic factor in sporadic amyotrophic lateral sclerosis patients. *J. Neurol. Neurosurg. Psychiatry* **84**, 1365–1371 (2013).
41. Watanabe, H. et al. A rapid functional decline type of amyotrophic lateral sclerosis is linked to low expression of TTN. *J. Neurol. Neurosurg. Psychiatry* **87**, 851–858 (2016).
42. Yang, W. S. & Stockwell, B. R. Ferroptosis: death by lipid peroxidation. *Trends Cell Biol.* **26**, 165–176 (2016).
43. Radak, Z., Zhao, Z., Goto, S. & Koltai, E. Age-associated neurodegeneration and oxidative damage to lipids, proteins and DNA. *Mol. Aspects Med.* **32**, 305–315 (2011).
44. Reed, T. T. Lipid peroxidation and neurodegenerative disease. *Free Radic. Biol. Med.* **51**, 1302–1319 (2011).
45. Alves, C. J. et al. Gene expression profiling for human iPS-derived motor neurons from sporadic ALS patients reveals a strong association between mitochondrial functions and neurodegeneration. *Front Cell Neurosci.* **9**, 289 (2015).
46. Burkhardt, M. F. et al. A cellular model for sporadic ALS using patient-derived induced pluripotent stem cells. *Mol. Cell Neurosci.* **56**, 355–364 (2013).
47. Imamura, K. et al. The Src/c-Abl pathway is a potential therapeutic target in amyotrophic lateral sclerosis. *Sci. Transl. Med.* **9**, (2017).
48. Ravits, J. et al. Deciphering amyotrophic lateral sclerosis: what phenotype, neuropathology and genetics are telling us about pathogenesis. *Amyotroph. Lateral Scler. Frontotemporal Degener.* **14** (Suppl 1), 5–18 (2013).
49. Mackenzie, I. R. et al. Pathological TDP-43 distinguishes sporadic amyotrophic lateral sclerosis from amyotrophic lateral sclerosis with SOD1 mutations. *Ann. Neurol.* **61**, 427–434 (2007).
50. Borasio, G. D. et al. Dopaminergic deficit in amyotrophic lateral sclerosis assessed with [I-123] IPT single photon emission computed tomography. *J Neurol Neurosurg. Psychiatry* **65**, 263–265 (1998).
51. Cooper, R. L. & Neckameyer, W. S. Dopaminergic modulation of motor neuron activity and neuromuscular function in *Drosophila melanogaster*. *Comp. Biochem. Physiol. B Biochem. Mol. Biol.* **122**, 199–210 (1999).
52. Yuan, N. & Lee, D. Suppression of excitatory cholinergic synaptic transmission by *Drosophila* dopamine D1-like receptors. *Eur. J. Neurosci.* **26**, 2417–2427 (2007).
53. Reimer, M. M. et al. Dopamine from the brain promotes spinal motor neuron generation during development and adult regeneration. *Dev. Cell* **25**, 478–491 (2013).
54. Simpson, E. P., Henry, Y. K., Henkel, J. S., Smith, R. G. & Appel, S. H. Increased lipid peroxidation in sera of ALS patients: a potential biomarker of disease burden. *Neurology* **62**, 1758–1765 (2004).
55. Chen, L., Hambright, W. S., Na, R. & Ran, Q. Ablation of the ferroptosis inhibitor glutathione peroxidase 4 in neurons results in rapid motor neuron degeneration and paralysis. *J. Biol. Chem.* **290**, 28097–28106 (2015).

Acknowledgements

The authors would like to thank W. Akamatsu (Juntendo University), D. Sipp, S. Morimoto, and Y. Nishimoto (Keio University) for providing invaluable comments on the project and all the members of the H.O. laboratory for their encouragement and kind support. We would also like to thank H. Inoue, S. Yamanaka, and M. Nakagawa (Kyoto University) for donating hiPSC clones (A21412, A21428, A3411, A3416, and 201B7) and M. Ishikawa (Keio University) for constructing and providing the existing drug library. This work was supported by funding from the Research Project for Practical Applications of Regenerative Medicine from the Japan Agency for Medical Research and Development (AMED) (grant nos. 15bk0104027h0003, 16bk0104016h0004, and 17bk0104016h0005 to H.O.), the Research Center Network for Realization Research Centers/Projects of Regenerative Medicine (the Program for Intractable Disease Research Utilizing Disease-specific iPS Cells and the Acceleration Program for Intractable Diseases Research Utilizing Disease-specific iPS Cells) from AMED (grant nos. 15bm0609003h0004, 16bm0609003h0005, 17bm0609003h0006 and 17bm0804003h0001 to H.O.), the research grants for the sporadic ALS patients registry study (JaCALS) from AMED (grant no. 17lk0201057h0002 to G.S.), a research grant on "Development of therapy for sporadic ALS from omics analyses using a large-scale clinical database, genomic DNA and immortalized cell repository of Japanese ALS patients from AMED" (grant no. 18ek0109284s0302 to G.S. and H.O.), an IBC grant from the Japan ALS Association (to H.O.), the Translational Research Network Program from AMED (to H.O.), the Practical Research Project for Rare/Intractable Diseases from AMED (grant nos. 18ek0109284s0302 to G.S. and H.O. and 18ek0109329h0001 to H.O.), the grant-in-aid project Scientific Research on Innovation Area (Brain Protein Aging and Dementia Control) from the Ministry of Education, Culture, Sports, Science and Technology of Japan (to G.S.and H.O.), Research Fellowships of the Japan Society for the Promotion of Science for Young Scientists (grant no. JP16J06437 to K.F.), the Keio University Grant-in-Aid for the Encouragement of Young Medical Scientists (to K.F.), and the Keio University Doctorate Student Grant-in-Aid Program (to K.F.).

Author contributions

K.F. and H.O. designed the study. K.F., A.O., and S.H. established motor neuron differentiation protocols. K.F. generated iPSCs from 32 SALS patients, analyzed the in vitro pathology of FALS and SALS models, designed the phenotype-based clustering system, performed drug screening, conducted in vitro pharmacology, performed transcriptome analysis, and analyzed the data. K.F. and H.S. designed the drug screening system. M.I. established iPSCs from ALS patients carrying *SOD1* mutations. N.A., R.N., T.A., M.A., and G.S. provided ALS patient samples and analyzed the data from clinical observations. H.S. provided the existing drug library for screening. Project management was conducted by S.H., M.A., H.S., G.S., and H.O. The manuscript was prepared by K.F. and H.O. All authors contributed to the final editing and approval of the manuscript.

Competing interests

H.O. is a paid Scientific Advisory Board Member at SanBio Co., Ltd. and K Pharma Inc.

Additional information

Supplementary information is available for this paper at https://doi.org/10.1038/s41591-018-0140-5.

Reprints and permissions information is available at www.nature.com/reprints.

Correspondence and requests for materials should be addressed to H.O.

Publisher's note: Springer Nature remains neutral with regard to jurisdictional claims in published maps and institutional affiliations.

Methods

Culture of undifferentiated iPSCs. The control human iPSC (hiPSC) lines 201B7[56], WD39[57], and 409B2[23]; the *FUS*-mutated familial ALS-iPSC lines FALS-e46, FALS-e48, FALS-e54, FALS-2e2, FALS-2e3, and FALS-2e23[23]; the *TDP-43*-mutated familial ALS-iPSC lines A21412, A21428, A3411, and A3416[58]; the SOD1-mutated familial ALS-iPSC lines 1-SOD1-4, 1-SOD1-6, 2-SOD1-1, 2-SOD1-4, 3-SOD1-1, 3-SOD1-4, and 3-SOD1-7; and the sporadic ALS-iPSC lines SALS-1, -2, -3, -4, …, and SALS-32 (32 total lines) were cultured with mitomycin C-treated SNL murine fibroblast feeder cells in standard hESC medium (Sigma-Aldrich) containing 20% knockout serum replacement (KSR) (Thermo Fisher), 0.1 mM non-essential amino acids (Sigma-Aldrich), 0.1 mM 2-mercaptoethanol (Sigma-Aldrich), and 4 ng ml^{-1} fibroblast growth factor 2 (FGF-2) (PeproTech) in an atmosphere containing 3% CO_2. The details of the healthy donors, FALS patients, and SALS patients; the iPSCs established from them; and isogenic iPSCs are provided in the Life Sciences Reporting Summary and Supplementary Tables 2 and 3. All experimental procedures for iPSCs derived from patients were approved by the Keio University School of Medicine Ethics Committee (approval no. 20080016).

Isolation of human T cells and generation of iPSCs. Peripheral blood mononuclear cells (PBMCs) were obtained from three ALS patients carrying the *SOD1* mutations 1-SOD1 (gene mutation: H46R, race: Japanese, sex: female, age: 37 years), 2-SOD1 (gene mutation: H46R, race: Japanese, sex: female, age: 45 years), and 3-SOD1 (gene mutation: H43R, race: Japanese, sex: male, age: 63 years) by centrifuging heparinized blood over Ficoll-Paque PREMIUM (GE Healthcare) according to the manufacturer's instructions. PBMCs were seeded on a plate with and cultured at 37 °C in 5% CO_2 in GT-T502 medium (KOHJIN BIO) containing 175 JRU ml^{-1} rIL-2 and Dynabeads Human T-Activator CD3/CD28 (Thermo Fisher). After 5 days of culture, activated PBMCs and activated T cells were transferred to a 96-well plate at a density of 1.5×10^3 cells per well and incubated for an additional 24 h. T cell lines (2×10^6 cells) were electroporated with pCE-hOCT3/4, pCE-hSK, pCE-hUL, pCE-mp53DD, and pCXB-EBNA1 (Addgene) using a Nucleofector 2D Device (Lonza) with the Amaxa Human T cell Nucleofector Kit (Lonza). At 24 h post-electroporation, the medium was replaced with fresh GT-T502 medium. At 48 h post-electroporation, the cells were collected and transferred to a 100-mm dish containing mitomycin C-inactivated SNL feeder cells. After an additional 24 h, the medium was replaced with hiPSC medium, which was changed every other day until colonies were selected. The generated hiPSCs were maintained on mitomycin C-inactivated SNL feeder cells in hiPSC medium. Established hiPSCs carrying *SOD1* mutations, specifically 1-SOD1-4, 1-SOD1-6, 2-SOD1-1, 2-SOD1-4, 3-SOD1-1, 3-SOD1-4, and 3-SOD1-7, were cultured, and cells at passage numbers between 5 and 18 were used for analysis. All experimental procedures for iPSCs including blood sampling from donors were approved by the Keio University School of Medicine Ethics Committee (approval no. 20080016).

Human iPSC generation from 32 LCLs from SALS patients. LCLs from 32 SALS patients, collected via a multicenter registration and follow-up system in Japan, JaCALS[39–41], were provided by Nagoya University. These LCLs were cultured in RPMI 1640 (Thermo Fisher) medium supplemented with 10% FBS at 37 °C and 5% CO_2 in a humidified incubator. After several passages, the LCLs were transfected using Sendai virus vectors (Cytotune 2.0; ID Pharma) expressing four factors (*OCT4*, *SOX2*, *KLF4*, and *c-MYC*) according to the manufacturer's instructions. At 24 h after infection, the infected LCLs were transferred to a 24-well plate containing mitomycin C-inactivated mouse SNL feeder cells at a density of 5.0×10^4–5.0×10^5 cells per dish and incubated for 24 h with mixed medium (RPMI 1640/hiPSC medium = 1/1). At 48 h after infection, the medium was replaced with hiPSC medium, and the culture medium was changed every other day. The generated hiPSCs were maintained with mitomycin C-inactivated mouse SNL feeder cells in hiPSC medium. These established SALS-iPSCs were cultured in bulk without colony selection and were used for subsequent analysis. The details of the SALS-iPSCs and SALS patients are provided in the Life Sciences Reporting Summary and Supplementary Table 3. All experimental procedures for iPSCs derived from patients were approved by the Keio University School of Medicine Ethics Committee (approval no. 20080016).

Motor neuron induction in vitro. For in vitro differentiation, hPSCs were cultured in hiPSC medium supplemented with 3 μM SB431542 (Tocris Bioscience), 3 μM dorsomorphin (Sigma-Aldrich), and 3 μM CHIR99021 (Stemgent) for 5 days. The medium was changed every day. On day 5, hPSC colonies were detached from the feeder layers using a dissociation solution (0.25% trypsin, 100 μg ml^{-1} collagenase IV (Thermo Fisher), 1 mM $CaCl_2$, and 20% KSR) and were enzymatically dissociated into single cells using TrypLE Select (Thermo Fisher). The dissociated cells were cultured in suspension at a density of 1×10^5 cells per ml in ultra-low attachment culture dishes (Corning) in MPC induction medium consisting of serum-free medium (media hormone mix; MHM) supplemented with 2% B27 supplement (Thermo Fisher), 20 ng ml^{-1} FGF, 10 ng ml^{-1} hLIF (Millipore), 2 μM SB431542, 3 μM CHIR99021, 2 μM retinoic acid (RA; Sigma-Aldrich), and 1 μM purmorphamine (Calbiochem) in a hypoxic and humidified atmosphere (4% O_2, 5% CO_2) for 7 days. Formed spheres were passaged by dissociation into single cells and then cultured in slightly modified MPC medium, MHM supplemented with 2% B27 supplement, 2 ng ml^{-1} bFGF, 10 ng ml^{-1} hLIF, 2 μM SB431542, 2 μM RA, and 1 μM purmorphamine for 7 days under 4% O_2 hypoxic conditions. DAPT (Sigma-Aldrich) was added to the modified MPC medium after 4 days from sphere passage (DIV16), with the final concentration adjusted to 5 μM. The medium was changed every 2–3 days for a total of 14 days to induce MPCs. The medium was changed every 2–3 days for a total of 14 days to induce MPCs.

To differentiate neuronal cells, dissociated MPCs were plated onto 96-well plates or coverslips 10 mm in diameter coated with poly-L-ornithine (PO) and growth-factor-reduced Matrigel (50× dilution, thin coated; Corning) and cultured in differentiation medium that consisted of MHM supplemented with 2% B27 supplement, 10 ng ml^{-1} rhBDNF (R&D Systems), 10 ng ml^{-1} rhGDNF (R&D Systems), 200 ng ml^{-1} ascorbic acid (Sigma-Aldrich), 1 μM RA, and 2 μM DAPT (Sigma-Aldrich) for 5–50 days in a humidified atmosphere of 5% CO_2. Half of the medium was changed every 1 or 2 days.

Time-course analysis of neurite outgrowth. For the time-course analysis of neurite length using iPSC-derived motor neuron culture, living motor neurons cultured in a multi-well plate were imaged via a live cell screening system BioStation CT (Nikon Instruments); a set of 5 × 5 fields was collected from each well using the 10× objective, resulting in over 15,000 cells being scored per well. Time-lapse imaging was performed over 60 days, and the imaging interval was 12 h. Analysis (CL-Quant; Nikon Instruments) began by identifying intact neural nuclei stained by Hoechst 33258 (0.5 μg ml^{-1}; Sigma-Aldrich), which were defined as traced nuclei that were larger than 50 μm^2 within cells with fiber object-like neurites. Neuronal cells were defined by their morphology and the contrast difference with the background, and the lengths of their fiber objects were quantified. Neurite length per neuronal cell was calculated from the sum of fiber object length and the total number of neuronal nuclei, and normalized by the data at DIV20.

Immunocytochemistry. Cells were fixed in phosphate-buffered saline (PBS) containing 4% paraformaldehyde (PFA) for 30 min at room temperature. Thereafter, all cells were blocked with 5% FBS and Triton X-100 and incubated with the primary antibodies described in Supplementary Table 4. The cells were then rinsed with PBS and incubated with species-specific Alexa Fluor 488-, Alexa Fluor 555-, or Alexa Fluor 647-conjugated secondary antibodies (1/1,000; Thermo Fisher), followed by staining with Hoechst 33258 (0.5 μg ml^{-1}; Sigma-Aldrich) to counterstain the nuclei. Images were obtained using an Axioplan2 (Carl Zeiss AG), LSM-710 (Carl Zeiss AG), BZ9000 (Keyence), or IN Cell Analyzer 6000 (GE Healthcare). The details of primary and secondary antibodies are described in the Life Sciences Reporting Summary.

High-content analysis. For cell population assays, fluorescence intensity analysis, neurite length analysis, apoptosis analysis, and ROS production assays, stained plates were imaged using the high-content cellular analysis system IN Cell Analyzer 6000; a set of 5 × 5 fields was collected from each well using the 20× objective, resulting in over 10,000 cells being scored per well. For FUS mislocalization analysis, FUS aggregate analysis, neurite swelling analysis, pTDP-43 inclusion analysis, stress granule analysis, and mitochondrial function assays, stained plates were imaged with the IN Cell Analyzer 6000; a set of 6 × 6 fields was collected from each well using the 60× objective, resulting in over 9,000 cells being scored per well. Analysis (IN Cell Developer Toolbox v1.9; GE Healthcare) began by identifying intact Hoechst-stained nuclei, which were defined as traced nuclei that were larger than 50 μm^2 in surface area and with intensity levels that were typical and lower than the threshold brightness of pyknotic cells. Each traced nucleus region was then expanded by 50% and cross-referenced with pluripotent markers (SSEA4 and TRA-1-60), an endodermal marker (AFP), a mesodermal marker (αSMA), an ectodermal marker (βIII-TUBULIN), an MPC marker (OLIG2), a neuron marker (βIII-TUBULIN, NeuN), a glia marker (GFAP), motor neuron markers (HB9, SMI-32, and ChAT), and dopaminergic neuron markers (TH and DAT) for identification; from these images, the percentage of each marker was calculated (for neural subtype markers stained as granules, the number of βIII-TUBULIN$^+$ cells containing one or more of the markers was quantified). By setting areas based on each neural subtype, the ratio of neurons with swelling, the ratio of FUS mislocalization into the cytosol (sum of cytoplasmic FUS$^+$ area / sum of cytoplasmic βIII-TUBULIN$^+$ area), the number of FUS, TDP-43, and SOD1 aggregates in neurons (no. of FUS$^+$, TDP-43$^+$, or SOD1$^+$ aggregates / no. of βIII-TUBULIN$^+$ cells), the number of stress granules with FUS and TDP-43 proteins in neurons (no. of FUS$^+$G3BP$^+$ or TDP-43$^+$G3BP$^+$ aggregates / no. of βIII-TUBULIN$^+$ cell), the number of pTDP-43 inclusions in neurons (no. of pTDP-43$^+$ aggregates / no. of βIII-TUBULIN$^+$ cells), or residual mitochondrial area in neurons (sum of cytosolic Tom20$^+$ area /sum of cytoplasmic βIII-TUBULIN$^+$ area) were analyzed. Using the above-described traced images of each cell, neurite length (sum of βIII-TUBULIN$^+$ fiber length / no. of βIII-TUBULIN$^+$ cells), CC3-positive cell ratio (no. of CC3$^+$β III-TUBULIN$^+$ cells / no. of βIII-TUBULIN$^+$ cells), and CellROX fluorescence intensity in neurons (sum of CellROX intensity in βIII-TUBULIN$^+$ cells / no. of β III-TUBULIN$^+$ cells) were also analyzed.

Multi-phenotypic screening. The compounds used in the drug screens were part of the Existing Drug Library (1232 compounds) from the Institute for Advanced Medical Research at the Keio University School of Medicine. For the primary screen, motor neurons from *FUS*-ALS iPSCs (FALS-2e3 and FALS-2e23) at DIV 40 were treated with vehicle alone (0.05% (v/v) DMSO) as a control or drug dissolved in DMSO or water at a concentration of 10 μM. After 120 h, culture supernatants were collected, and the cells were fixed and labeled with antibodies against FUS, G3BP, and βIII-TUBULIN. Using collected supernatants and immunostained cells, neurite lengths (sum of βIII-TUBULIN$^+$ fiber length / no. of βIII-TUBULIN$^+$ cells), the number of formed stress granules (no. of G3BP$^+$ aggregates / no. of β III-TUBULIN$^+$ cell) and leaked FUS aggregates (no. of cytosolic FUS$^+$ aggregates / no. of βIII-TUBULIN$^+$ cells), and the relative amount of LDH leakage (sum of leaked LDH intensity in *FUS*-ALS models / sum of leaked LDH intensity in healthy donor models) were measured and evaluated as endpoints of drug efficacy using the IN Cell Analyzer 6000 and iMark Microplate Absorbance Reader (BioRad). Experimental data for the tested drugs were normalized to the DMSO control (set value of 1) on a per-plate basis. For secondary screening, 95 compounds selected from the primary screen were used to treat motor neurons from *TDP-43*-ALS models at DIV 35 at concentrations of 0.1, 1, and 10 μM. The decrease in neurite length (sum of βIII-TUBULIN$^+$ fiber length / no. of βIII-TUBULIN$^+$ cells), pTDP-43 aggregation (no. of pTDP-43$^+$ aggregates / no. of βIII-TUBULIN$^+$ cells), increase in CC3 ratio (no. of CC3$^+$βIII-TUBULIN$^+$ cells / no. of βIII-TUBULIN$^+$ cells), and the amount of LDH leakage (sum of leaked LDH intensity in *TDP-43*-ALS models / sum of leaked LDH intensity in healthy donor models) were measured and evaluated as endpoints of drug efficacy. In both primary and secondary screens, the following selection criteria were used for compounds that quantitatively exhibited pathological suppressive reactivity compared with the DMSO control (set value of 1) for all endpoints: neurite length >1, apoptosis <1, number of stress granules <1, abnormal protein aggregates <1, and cell damage <1.

Case clustering with in vitro disease progression. Hierarchical cluster analysis was performed based on Euclidean distances and Ward clustering with R software using the following datasets from iPSC-derived motor neurons from 32 SALS patients: the shifting time point of neurite outgrowth toward a negative and significant increase in leaked LDH compared to that of healthy donors and the time-dependent alteration patterns of neurite length and leaked LDH. The shifting time point of neurite outgrowth was identified based on the neurite length change rate every 5 days, as quantified by a BioStation CT (Nikon Instruments).

Three-dimensional case distributions with characterized phenotype and disease progress in vitro. A principal component analysis (PCA) was performed and visualized with the k-means clustering algorithm in R software using the following datasets from iPSC-based motor neurons from healthy donors, *SOD1*-FALS, *FUS*-FALS, *TDP-43*-FALS, SALS, and ROPI-treated cells: the quantification data from abnormal protein aggregations characterized by specific genetic mutations of FALS (the number (1) and the area (2) of SOD1$^+$, FUS$^+$, and/or TDP-43$^+$aggregates), the shifting time point of neurite outgrowth toward a negative (3) and significant increase in leaked LDH (4) compared with healthy donors, and the time-dependent alteration patterns of neurite length (5) and leaked LDH (6). Regarding components (1) and (2), the number of FUS, TDP-43, or SOD1 aggregates per neuron (no. of FUS$^+$, TDP-43$^+$, or SOD1$^+$ aggregates / no. of βIII-TUBULIN$^+$ cells) and the area of their aggregates in the neuronal cytoplasm (sum of cytoplasmic FUS$^+$, TDP-43$^+$, or SOD1$^+$ aggregates area / sum of cytoplasmic βIII-TUBULIN$^+$ area) were quantified with the IN Cell Developer Toolbox v1.9 (GE Healthcare). These phenotype scores of SALS were quantified/normalized by the value of *FUS*-, *TDP-43*-, or *SOD1*-ALS models. Regarding components (3) and (4), the numerical variation rates of neurite length (sum of βIII-TUBULIN$^+$ fiber length / no. of βIII-TUBULIN$^+$ cells) and leaked LDH (sum of leaked LDH intensity in ALS models / sum of leaked LDH intensity in healthy donor models) were normalized by each dataset at DIV20, and calculated by dividing the culture period every 5 days. The time phase in which these 5-day numerical values showed a significant difference as compared with the datasets of healthy donors was identified. Regarding components (5) and (6), numerical variations were patterned by normalizing each dataset at DIV20, and the rate of change at each DIV were used for PCA. The shifting time point of neurite outgrowth was quantified by the BioStation CT (Nikon Instruments).

Phenotype scoring of SALS pathologies. The scoring of SALS pathologies was performed by focusing on the number of aggregates and the localization of the FUS, TDP-43, and SOD1 proteins, which are characteristic of *FUS*-, *TDP-43*-, and *SOD1*-ALS, respectively. Using co-stained images showing one of the above three characterized proteins along with βIII-TUBULIN and Hoechst 33258, the Hoechst stain was removed from the merged image to obtain a neuronal cytoplasmic image. (When motor-neuron-specific analysis was performed, HB9$^+$βIII-TUBULIN$^+$ cells were extracted in advance using HB9-stained images.) The number of FUS, TDP-43, or SOD1 aggregates per neuron (no. of FUS$^+$, TDP-43$^+$, or SOD1$^+$ aggregates / no. of βIII-TUBULIN$^+$ cells) and the area of their aggregates in the neuronal cytoplasm (sum of cytoplasmic FUS$^+$, TDP-43$^+$, or SOD1$^+$ aggregates area / sum of cytoplasmic βIII-TUBULIN$^+$ area) were quantified with the IN Cell Developer Toolbox v1.9 (GE Healthcare). The measured values of each phenotype from the *FUS*-, *TDP-43*-, and *SOD1*-ALS models, which acted as positive controls for each phenotype, were normalized as 1, and the above two phenotypes, the number and the area of FUS, TDP-43, or SOD1 aggregates, were integrated; therefore, the maximum value was 2 (reference value of the phenotype score). Using this baseline, the phenotype score was calculated for each FALS-expressed protein in 32 SALS models. By estimating 32 SALS phenotype scores and averaging them, the averaged phenotype score was calculated for each protein characterized in FALS.

Phenotype rescue by drug treatment. To evaluate the efficacy of the screened drug candidates for ALS therapeutics using SALS models, four ALS phenotypes were used as endpoints: (1) neurite regression (sum of βIII-TUBULIN$^+$ fiber length / no. of βIII-TUBULIN$^+$ cells), (2) apoptosis (no. of CC3$^+$βIII-TUBULIN$^+$ cells / no. of βIII-TUBULIN$^+$ cells), (3) abnormal protein aggregates (no. of FUS$^+$ or TDP-43$^+$ aggregates / no. of βIII-TUBULIN$^+$ cells), and (4) cytotoxicity (sum of leaked LDH intensity in ALS models / sum of leaked LDH intensity in healthy donor models). For the efficacy evaluation of drug candidates, the value of untreated-ALS was set as 0 and that of healthy donor was set as 100 in each of these four phenotypes. Drug efficacy was evaluated as "% of phenotype rescue"; how much the value of the drug-treated ALS approached that of a healthy donor. To adjust the maximum value of phenotype rescue to 100 when accumulating four endpoints, the upper limit of phenotype rescue for each item was compressed to 25.

Transcriptome analysis. One sample per line was prepared from three independent inductions. Total RNA was extracted with an RNeasy Kit (QIAGEN), and RNA quality was assessed using an NanoDrop 1000 (Thermo Fisher). Total RNA (100 ng) was reverse transcribed, labeled with biotin using a 3'IVT Express Kit (Affymetrix), and hybridized to a GeneChip® Human Genome U133 plus 2.0 Array (Affymetrix). The arrays were washed and stained using a GeneChip Fluidics Station 450 (Affymetrix) and then scanned with the GeneChip Scanner 3000 7 G System (Affymetrix) according to the manufacturer's instructions. The raw probe intensity files were MAS5-normalized and log (base2) transformed by using Expression Console software (Affymetrix). The gene set was filtered based on expression levels to remove genes that were not expressed in all samples. PCA was performed using the normalized data. For hierarchical clustering, the normalized data were calculated based on Euclidean correlations with average linkages. Analysis and data visualization of the transcripts were performed with Subio Platform software (Subio). Visualization of gene network using the extracted gene set were performed by GeneMANIA online tool (https://genemania.org/).

The data discussed in this publication have been deposited into the NCBI Gene Expression Omnibus (GEO, http://www.ncbi.nlm.nih.gov/geo/) database and are accessible with GEO Series accession number GSE106382.

Mitophagy analysis under stress conditions. Motor neurons were cultured with 30 μM carbonyl cyanide m-chlorophenyl hydrazone (CCCP; Sigma-Aldrich), 10 μM L-glutamate (L-Glu; Sigma-Aldrich), DMSO, or PBS for 48 h. The cells were then fixed, stained for βIII-TUBULIN and Tom20, and counterstained with Hoechst. The mitochondrial area of the neuronal cytoplasm was extracted and quantified from the digitized values using an IN Cell Analyzer 6000.

Analysis of mitochondrial activity. An MTT Cell Viability Assay Kit (BioAssay Systems) was used to evaluate the cell viability of hiPSC-derived motor neurons. In all experiments, single-cell dissociated MPCs were seeded into 96-well plates at a density of 1.5×10^5 cells per cm^2 per well. At 5 days after MPC seeding, an MTT assay was performed every fifth day according to the manufacturer's protocol. MTT (15 μl per well) was added to the wells and incubated at 37 °C for 4 h. The supernatant was removed, and 100 μl of solubilizer was added per well to dissolve the produced formazan. After shaking the plates for 10 min, the absorbance values of the wells were recorded with a microplate reader at a wavelength of 570 nm.

Analysis of lipid peroxidation. Lipid peroxidation was measured as the level of MDA determined by the thiobarbituric acid reaction following the manufacturer's instructions (TBARS Assay Kit, Cayman). The absorbance was measured at 540 nm. The concentration of MDA was expressed as μM of MDA per mg of protein using an iMark Microplate Absorbance Reader. The quantified MDA in the lysate was corrected by the number of neurons measured by the IN Cell Analyzer 6000 before this analysis. Using this score in the healthy donor group as a reference value, the relative values of the SALS group were represented as lipid peroxidation scores.

Quantitative RT–PCR. Total RNA was isolated with an RNeasy mini kit (QIAGEN) with DNase I treatment, and cDNA was prepared by using a ReverTra Ace qPCR RT kit (Toyobo). Quantitative RT–PCR was performed using SYBR Premix Ex Taq II (Takara Bio) on a ViiA 7 Real-Time PCR System (Life Technologies). The details of qRT–PCR primers are described in Supplementary Table 4.

Statistical analyses. Values are expressed as mean ± s.d. Statistical significance was calculated with GraphPad Prism (GraphPad Software) or Subio Platform software

(Subio). The effect of the treatments on the cell lines was analyzed using a two-tailed paired *t*-test. A two-tailed non-paired *t*-test was used to compare differences between two groups, and one-way ANOVA followed by Dunnett's or Tukey's multiple comparisons test were used to compare three or more groups. Two-tailed Fisher's exact test was used for the pathway/gene ontology enrichment analysis. *P*-values less than 0.05 were considered significant differences.

Compliance with relevant ethical regulations. All experimental protocols and procedures were in compliance with the university and institutional ethical regulations.

Reporting Summary. Further information on experimental design is available in the Nature Research Reporting Summary linked to this article.

Data availability. Microarray data have been deposited in the GEO under accession GSE106382. The data supporting the findings of the current study are available from the corresponding author upon reasonable request.

References

56. Takahashi, K. et al. Induction of pluripotent stem cells from adult human fibroblasts by defined factors. *Cell* **131**, 861–872 (2007).
57. Imaizumi, Y. et al. Mitochondrial dysfunction associated with increased oxidative stress and alpha-synuclein accumulation in PARK2 iPSC-derived neurons and postmortem brain tissue. *Mol. Brain* **5**, 35 (2012).
58. Egawa, N. et al. Drug screening for ALS using patient-specific induced pluripotent stem cells. *Sci. Transl. Med.* **4**, 145ra104 (2012).

nature research

Corresponding author(s): Hideyuki Okano

Life Sciences Reporting Summary

Nature Research wishes to improve the reproducibility of the work that we publish. This form is intended for publication with all accepted life science papers and provides structure for consistency and transparency in reporting. Every life science submission will use this form; some list items might not apply to an individual manuscript, but all fields must be completed for clarity.

For further information on the points included in this form, see Reporting Life Sciences Research. For further information on Nature Research policies, including our data availability policy, see Authors & Referees and the Editorial Policy Checklist.

Please do not complete any field with "not applicable" or n/a. Refer to the help text for what text to use if an item is not relevant to your study.

For final submission: please carefully check your responses for accuracy; you will not be able to make changes later.

Experimental design

1. Sample size

Describe how sample size was determined.

Sample size was determined based on our previous experience and the work of other groups using stem cells as experimental model systems.

2. Data exclusions

Describe any data exclusions.

No data were excluded.

3. Replication

Describe the measures taken to verify the reproducibility of the experimental findings.

All the experimental data were replicated at least in three independent experiments. The experimental findings were reliably reproduced.

4. Randomization

Describe how samples/organisms/participants were allocated into experimental groups.

Samples were randomly allocated to control and experimental groups.

5. Blinding

Describe whether the investigators were blinded to group allocation during data collection and/or analysis.

The investigators were not blinded to group allocation. Multiple iPSC lines were used in each experiment, including 1,232 drug-screening experiment. Blinding could easily bring in confusions/mistakes across experiments and among investigators. The screened compounds layout and their details were disclosed after completion of the secondary screening.

Note: all in vivo studies must report how sample size was determined and whether blinding and randomization were used.

6. Statistical parameters

For all figures and tables that use statistical methods, confirm that the following items are present in relevant figure legends (or in the Methods section if additional space is needed).

n/a	Confirmed
☐	☒ The exact sample size (*n*) for each experimental group/condition, given as a discrete number and unit of measurement (animals, litters, cultures, etc.)
☐	☒ A description of how samples were collected, noting whether measurements were taken from distinct samples or whether the same sample was measured repeatedly
☐	☒ A statement indicating how many times each experiment was replicated
☐	☒ The statistical test(s) used and whether they are one- or two-sided *Only common tests should be described solely by name; describe more complex techniques in the Methods section.*
☐	☒ A description of any assumptions or corrections, such as an adjustment for multiple comparisons
☐	☒ Test values indicating whether an effect is present *Provide confidence intervals or give results of significance tests (e.g. P values) as exact values whenever appropriate and with effect sizes noted.*
☐	☒ A clear description of statistics including central tendency (e.g. median, mean) and variation (e.g. standard deviation, interquartile range)
☐	☒ Clearly defined error bars in all relevant figure captions (with explicit mention of central tendency and variation)

See the web collection on statistics for biologists for further resources and guidance.

Software

Policy information about availability of computer code

7. Software

Describe the software used to analyze the data in this study.	- Immunocytochemistry and drug screening: analyzed with IN Cell Developer Toolbox v1.9 (GE Healthcare) and/or Microplate Manager6 (Bio-Rad) - Time course analysis of neurite outgrowth: analyzed with CL-Quant (version 3.10; Nikon Instruments) - Statistical analyses : analyzed with GraphPad Prism (version 6; GraphPad Software) - RNA quality assessment : analyzed with NanoDrop 1000 software (version 3.8.1; Thermo Fisher) - Probe set summarization and CHP file generation for 3' expression: analyzed with Expression Console software (version 1.4; Affymetrix) - Transcriptome analyses : analyzed with Subio Platform (version 1.21.5054; Subio) and GeneMania online tool - Phenotype-based case clusterings: analyzed with R software - qPCR analyses : analyzed with ViiA7 software (version 1.2.4; Thermo Fisher)

For manuscripts utilizing custom algorithms or software that are central to the paper but not yet described in the published literature, software must be made available to editors and reviewers upon request. We strongly encourage code deposition in a community repository (e.g. GitHub). *Nature Methods* guidance for providing algorithms and software for publication provides further information on this topic.

Materials and reagents

Policy information about availability of materials

8. Materials availability

Indicate whether there are restrictions on availability of unique materials or if these materials are only available for distribution by a third party.	There are no restrictions on availability of unique materials

9. Antibodies

Describe the antibodies used and how they were validated for use in the system under study (i.e. assay and species).

The following antibodies were used:
Mouse anti-TRA-1-60, MAB4360, Millipore (1:1000)
Mouse anti-SSEA4, ab16287, Abcam (1:1000)
Rabbit anti-SSEA4, Bs-3609R, Bioss (1:1000)
Goat anti-OLIG2, AF2418, R&D Systems (1:500)
Mouse anti-HB9, 81.5C10, DSHB (1:150)
Mouse anti-SMI32, SMI-32P, BioLegend (1:2500)
Sheep anti-ChAT, ab18736, Abcam (1:250)
Chicken anti-ChAT, CAT, Aves Labs (1:1000)
Rabbit anti-GFAP, Z033401, DAKO (1:4000)
Mouse anti-betaIII-TUBULIN, T8660, Sigma-Aldrich (1:1000)
Rabbit anti-NeuN, ab104225, Abcam (1:500)
Rabbit anti-VGLUT1, 135-303, Synaptic Systems (1:1000)
Rabbit anti-TH, AB152, Millipore, 1:500
Rat anti-DAT, ab5990, Abcam, 1:200
Rabbit anti-Cleaved Caspase-3, 9661, Cell Signaling Technology (1:500)
Rabbit anti-FUS, A300-293A, Bethyl Laboratories (1:1000)
Mouse anti-pTDP-43, TIP-PTD-M01, Cosmo Bio (1:500)
Rabbit anti-TDP-43, 10782-2-AP, Proteintech (1:500)
Chicken anti-G3BP, PA1-27843, Life Technologies (1:1000)
Mouse anti-G3BP, 611126, BD Bioscience (1:500)
Rabbit anti-TOM20, sc-11415, Santa Cruz Biotech (1:500)
Mouse anti-alphaSMA, A2547, Sigma-Aldrich (1:500)
Mouse anti-AFP, MAB1368, R&D Systems (1:200)
(This information is also included in Supplementary Table 4)
Alexa Fluor 488 Goat Anti-Rabbit IgG (H+L), A11034, Thermo Fisher (1:1000)
Alexa Fluor 555 Goat Anti-Rabbit IgG (H+L), A21429, Thermo Fisher (1:1000)
Alexa Fluor 647 Goat Anti-Rabbit IgG (H+L), A21245, Thermo Fisher (1:1000)
Alexa Fluor 488 Donkey Anti-Rabbit IgG (H+L), A21206, Thermo Fisher (1:1000)
Alexa Fluor 555 Donkey Anti-Rabbit IgG (H+L), A31572, Thermo Fisher (1:1000)
Alexa Fluor 647 Donkey Anti-Rabbit IgG (H+L), A31573, Thermo Fisher (1:1000)
Alexa Fluor 488 Goat Anti-Mouse IgG1, A21121, Thermo Fisher (1:1000)
Alexa Fluor 555 Goat Anti-Mouse IgG1, A21127, Thermo Fisher (1:1000)
Alexa Fluor 647 Goat Anti-Mouse IgG1, A21240, Thermo Fisher (1:1000)
Alexa Fluor 488 Goat Anti-Mouse IgG2a, A21131, Thermo Fisher (1:1000)
Alexa Fluor 555 Goat Anti-Mouse IgG2a, A21137, Thermo Fisher (1:1000)
Alexa Fluor 647 Goat Anti-Mouse IgG2a, A21241, Thermo Fisher (1:1000)
Alexa Fluor 488 Goat Anti-Mouse IgG2b, A21141, Thermo Fisher (1:1000)
Alexa Fluor 555 Goat Anti-Mouse IgG2b, A21147, Thermo Fisher (1:1000)
Alexa Fluor 647 Goat Anti-Mouse IgG2b, A21242, Thermo Fisher (1:1000)
Alexa Fluor 488 Donkey Anti-Goat IgG (H+L), A11055, Thermo Fisher (1:1000)
Alexa Fluor 555 Donkey Anti-Goat IgG (H+L), A21432, Thermo Fisher (1:1000)
Alexa Fluor 647 Donkey Anti-Goat IgG (H+L), A21447, Thermo Fisher (1:1000)
Alexa Fluor 488 Donkey Anti-Sheep IgG (H+L), A11015, Thermo Fisher (1:1000)
Alexa Fluor 568 Donkey Anti-Sheep IgG (H+L), A21099, Thermo Fisher (1:1000)
Alexa Fluor 488 Goat Anti-Chicken IgY (H+L), A11039, Thermo Fisher (1:1000)
Alexa Fluor 568 Goat Anti-Chicken IgY (H+L), A11041, Thermo Fisher (1:1000)
Alexa Fluor 488 Goat Anti-Rat IgG (H+L), A11006, Thermo Fisher (1:1000)

The subcellular localization of all the proteins analyzed in this study has been previously reported. This was used to validate the specificity of the antibody.

10. Eukaryotic cell lines

a. State the source of each eukaryotic cell line used.

The following cell lines were used:
Human induced pluripotent stem (iPS) cells:
- 201B7 (Healthy donor-derived iPSC) (kindly provided by Prof. Shinya Yamanaka and Dr. Masato Nakagawa, Center for iPS Cell Research and Application, Kyoto University, Japan)
- 409B2, WD39, LKA10, LKA29, and LKA36 (Healthy donors-derived iPSCs) (established in our previous studies)
- A21412, A21428, A3411, and A3416 (Familial ALS patients-derived iPSCs carrying TDP-43 mutations) (kindly provided by Prof. Haruhisa Inoue, Center for iPS Cell Research and Application, Kyoto University, Japan)
- FALS-e46, FALS-e48, FALS-e54, FALS-2e2, FALS-2e3, and FALS-2e23 (Familial ALS patients-derived iPSCs carrying FUS mutations, established in our previous study)
- 1SOD1-4, 1SOD1-6, 2SOD1-1, 2SOD1-4, 3SOD1-1, 3SOD1-4, and 3SOD1-7 (Familial ALS patients-iPSCs carrying SOD1 mutations, established in this study)
- FUS^H517D/H517D-1, FUS^H517D/H517D-2, and FUS^H517D/H517D-3 (Isogenic iPSCs carrying FUS mutations, established in our previous study)
Human lymphoblastoid B-cell lines (LCLs):
- SALS-1, SALS-2, SALS-3, ..., and SALS-32 (Sporadic ALS patients-derived LCLs)
(This information is also included in Supplementary Table 2 and 3)
Feeder cells: SNL 76/7 feeder cells (Wellcome Trust Sanger Institute)

b. Describe the method of cell line authentication used.

The pluripotency of our established iPSC lines were confirmed by immunofluorescence and in vitro differentiation assay into three germ layers. All of the tested iPSC lines had normal karyotypes.

c. Report whether the cell lines were tested for mycoplasma contamination.

Cell lines were routinely tested for mycoplasma contamination by MycoAlert (Lonza). All cell lines were negative for mycoplasma contamination.

d. If any of the cell lines used are listed in the database of commonly misidentified cell lines maintained by ICLAC, provide a scientific rationale for their use.

No commonly misidentified cell lines were used in the study.

Animals and human research participants

Policy information about studies involving animals; when reporting animal research, follow the ARRIVE guidelines

11. Description of research animals

Provide all relevant details on animals and/or animal-derived materials used in the study.

No animals were used in the study.

12. Description of human research participants

Describe the covariate-relevant population characteristics of the human research participants.

The following healthy persons and ALS patients provided their samples for iPSC establishment:
- Healthy donor-1, 36-year-old female, dermal fibroblasts
- Healthy donor-2, 16-year-old female, dermal fibroblasts
- Healthy donor-3, 40-year-old male, peripheral blood cells (LCLs)
- FUS-ALS patient-1, 39-year-old male, dermal fibroblasts
- FUS-ALS patient-2, 42-year-old male, dermal fibroblasts
- TDP-43-ALS patient-1, 55-year-old male, dermal fibroblasts
- TDP-43-ALS patient-2, 62-year-old male, dermal fibroblasts
- SOD1-ALS patient-1, 37-year-old male, peripheral blood cells
- SOD1-ALS patient-2, 45-year-old male, peripheral blood cells
- SOD1-ALS patient-3, 63-year-old male, peripheral blood cells

(This information is also included in Supplementary Table 2)
- Sporadic ALS patient-1, 60-year-old female, peripheral blood cells (LCLs)
- Sporadic ALS patient-2, 78-year-old male, peripheral blood cells (LCLs)
- Sporadic ALS patient-3, 37-year-old male, peripheral blood cells (LCLs)
- Sporadic ALS patient-4, 50-year-old male, peripheral blood cells (LCLs)
- Sporadic ALS patient-5, 39-year-old male, peripheral blood cells (LCLs)
- Sporadic ALS patient-6, 62-year-old male, peripheral blood cells (LCLs)
- Sporadic ALS patient-7, 59-year-old male, peripheral blood cells (LCLs)
- Sporadic ALS patient-8, 73-year-old male, peripheral blood cells (LCLs)
- Sporadic ALS patient-9, 40-year-old male, peripheral blood cells (LCLs)
- Sporadic ALS patient-10, 66-year-old female, peripheral blood cells (LCLs)
- Sporadic ALS patient-11, 56-year-old male, peripheral blood cells (LCLs)
- Sporadic ALS patient-12, 49-year-old male, peripheral blood cells (LCLs)
- Sporadic ALS patient-13, 51-year-old male, peripheral blood cells (LCLs)
- Sporadic ALS patient-14, 58-year-old female, peripheral blood cells (LCLs)
- Sporadic ALS patient-15, 55-year-old female, peripheral blood cells (LCLs)
- Sporadic ALS patient-16, 67-year-old male, peripheral blood cells (LCLs)
- Sporadic ALS patient-17, 60-year-old male, peripheral blood cells (LCLs)
- Sporadic ALS patient-18, 55-year-old male, peripheral blood cells (LCLs)
- Sporadic ALS patient-19, 60-year-old female, peripheral blood cells (LCLs)
- Sporadic ALS patient-20, 47-year-old male, peripheral blood cells (LCLs)
- Sporadic ALS patient-21, 39-year-old female, peripheral blood cells (LCLs)
- Sporadic ALS patient-22, 65-year-old female, peripheral blood cells (LCLs)
- Sporadic ALS patient-23, 61-year-old male, peripheral blood cells (LCLs)
- Sporadic ALS patient-24, 64-year-old female, peripheral blood cells (LCLs)
- Sporadic ALS patient-25, 65-year-old male, peripheral blood cells (LCLs)
- Sporadic ALS patient-26, 56-year-old female, peripheral blood cells (LCLs)
- Sporadic ALS patient-27, 37-year-old male, peripheral blood cells (LCLs)
- Sporadic ALS patient-28, 48-year-old female, peripheral blood cells (LCLs)
- Sporadic ALS patient-29, 48-year-old male, peripheral blood cells (LCLs)
- Sporadic ALS patient-30, 66-year-old female, peripheral blood cells (LCLs)
- Sporadic ALS patient-31, 47-year-old male, peripheral blood cells (LCLs)
- Sporadic ALS patient-32, 60-year-old male, peripheral blood cells (LCLs)

(This information is also included in Supplementary Table 3)